AN ABSTRACT OF THE THESIS OF

Logan J. Anspach for the degree of Master of Science in Radiation Health Physics presented on May 29, 2020.

Title: Development of a Fundamental Depth-Dependent Neutron Dosimetry Model

Abstract approved:

_____

David M. Hamby

Abstract:

Current neutron dosimetry methods rely on the assumption that charged particle equilibrium (CPE) is established within the tissue medium. This maintains that the kinetic energy transferred to the medium (KERMA) is equivalent to absorbed dose. However, this assumption is only valid for large volumes such as the whole body. For small volumes near the surface of the skin, CPE does not always exist. The aim of this study was to develop a deterministic, depth-dependent neutron dosimetry model that accounts for the lack in CPE at shallow depths. The bulk of the model was developed from first principles and existing neutron cross-sectional data. A series of simulations were constructed utilizing MCNP to investigate the relationship between KERMA and absorbed dose with depth in tissue. From this work, a method to account for fractional charged particle equilibrium is proposed and incorporated in a first principles neutron dosimetry model.

Development of a Fundamental Depth-Dependent Neutron Dosimetry Model

by

Logan J. Anspach

A THESIS

submitted to

Oregon State University

in partial fulfillment of

the requirements for the

degree of

Master of Science

Presented May 29, 2020

Commencement June 2020

Master of Science thesis of Logan J. Anspach presented on May 29, 2020

APPROVED:

Major Professor, representing Radiation Health Physics

Head of the School of Nuclear Science and Engineering

Dean of the Graduate School

I understand that my thesis will become part of the permanent collection of Oregon State University libraries. My signature below authorizes release of my thesis to any reader upon request.

Logan J. Anspach, Author

ACKNOWLEDGEMENTS

I would like to express my deepest gratitude to my advisor Dr. David Hamby for providing his continued support over these last four years. In every project that we have worked on together he has provided a wealth of insight and encouragement that has pushed me to become a better student, researcher, and health physicist. He is the best mentor I could have asked for; someday I hope to pay it forward.

I'd also like to thank Dr. David Boozer for the countless number of times I came to him with an MCNP or curve fitting question. He was always willing to take the time to walk me through these difficult subjects and provide unique perspectives that ultimately culminated in the simulations used within this report.

TABLE OF CONTENTS

TABLE OF CONTENTS (Continued)

LIST OF FIGURES

LIST OF TABLES

LIST OF APPENDICES

LIST OF APPENDIX FIGURES

Figure Page

LIST OF APPENDIX FIGURES (Continued)

Figure Page

DEDICATION

I would like to thank my parents, James and Deborah; your encouragement and support in every one of my undertakings is the reason I am here today. I must also acknowledge my siblings, Dylan and Megan, for their continued achievements and successes has made it difficult to claim that the first child is always best. Finally, I'd like to express my love and gratitude for my wonderful girlfriend, Abigale Hayes, for her continued moral support over these last six years.

1 Introduction

1.1 Overview

At the beginning of the 20th century the focus of the physics community was on the structure of the atom. Initially, J. J. Thomson theorized what is now known as the "Plum Pudding Model" wherein the atom is considered a sphere of positive charge evenly distributed with electrons. In 1911 Ernest Rutherford overturned this model following the Geiger-Marsden gold foil experiment, suggesting that the atom is primarily empty space with a concentrated positive nucleus. In 1930 Walther Bothe and Herbert Becker observed the production of "neutral radiation" following the bombardment of beryllium with alpha particles. Irene and Frederic Joliot-Curie observed that this unknown radiation produced 5.3 MeV protons within a paraffin target. James Chadwick recreated these experiments and observed the production of charged particles in other targets of hydrogen, nitrogen, and oxygen. Through the conservation of energy, he proved that these reactions were only possible if the neutral radiation was a particle with comparable mass to that of a proton. What had been observed was the elastic scatter of a neutron with hydrogen following (Nave, 2017):

$$ {}^{9}_{4}Be + {}^{4}_{2}He \rightarrow {}^{12}_{6}C + {}^{1}_{0}n $$

The discovery of the neutron was immediately seized upon to continue probing the structure of the nucleus, leading to the discovery of new elements, nuclides, and eventually nuclear fission. Since the 1930s neutrons have been used in industrial applications such as nuclear power, cancer therapy, and material

science. However, neutrons can also pose a significant health risk. Both Harry Daghlian and Louis Slotin succumbed to radiation poisoning following separate criticality accidents at Los Alamos National Laboratory with the same core of sub-critical plutonium on August 21st, 1945 and May 21st, 1946, respectively (Atomic Heritage Foundation, 2014).

While these events are a reminder of how dangerous neutrons can be in extraordinary scenarios, the primary concern for the industrial application of neutrons is cancer fatality. Both the National Council on Radiation Protection and Measurements (NCRP) and the International Commission on Radiological Protection (ICRP) recommend dose limits to occupational workers based on the Life Span Study, an epidemiological evaluation of fatal cancer risk among the 120,000 survivors of the Hiroshima and Nagasaki atomic bombings. Currently, the Nuclear Regulatory Commission (NRC) recommends that the total effective dose equivalent (whole body) and the dose equivalent to any organ cannot exceed 5 and 50 rem (0.05 and 0.5 Sv), respectively. Additionally, the NRC requires that the shallow-dose equivalent to the skin of the whole-body or of any extremity must not exceed 50 rem (0.5 Sv) and that it must reflect the highest dose received by any contiguous 10 cm^2 of skin (United States Nuclear Regulatory Commission, 2018).

A balance between safety and utility is the primary concern for health physicists throughout the industry. Rigid interpretation of the regulations is employed wherever neutron sources are utilized. As such, when exposures occur it is the duty of the health physicist to accurately account for dose to ensure the

wellbeing of workers. The aim of this research is to develop a useful method of neutron dosimetry to aid occupational health physicists and regulators in this task.

1.2 Research Objectives

This paper focuses on the development of a deterministic first-collision depth-dependent neutron dosimetry model. While much of the development is based on a first-principles approach, there are several complexities that are addressed/verified through Monte Carlo simulation, including such concepts as charged particle equilibrium in shallow tissue. Current neutron dosimetry methods rely on the assumption that KERMA is equivalent to dose. However, this is invalid for small tissue segments where analysis of the transfer of kinetic energy to heavy charged particles and their subsequent transmission through a tissue medium is required. As such, the depth-dose relationship between KERMA and absorbed dose is explored for mono-energetic neutrons over a wide range of energies. Several equations are fit to the resultant data to accurately described this relationship and an appropriate model depth-dependent neutron dosimetry model is proposed.

2 Background

2.1 Skin Physiology

The skin is the largest organ in the human body, comprising approximately 16% of total body weight. On average it is 2 mm thick and acts as a shield against the external environment, preventing infection. Additionally, it regulates body temperature, gathers sensory input, and stores water and fat. There are two main layers, the epidermis and the dermis. Below these layers is subcutaneous fat, an energy source for the body that varies in thickness depending on location (National Cancer Institute, 2018).

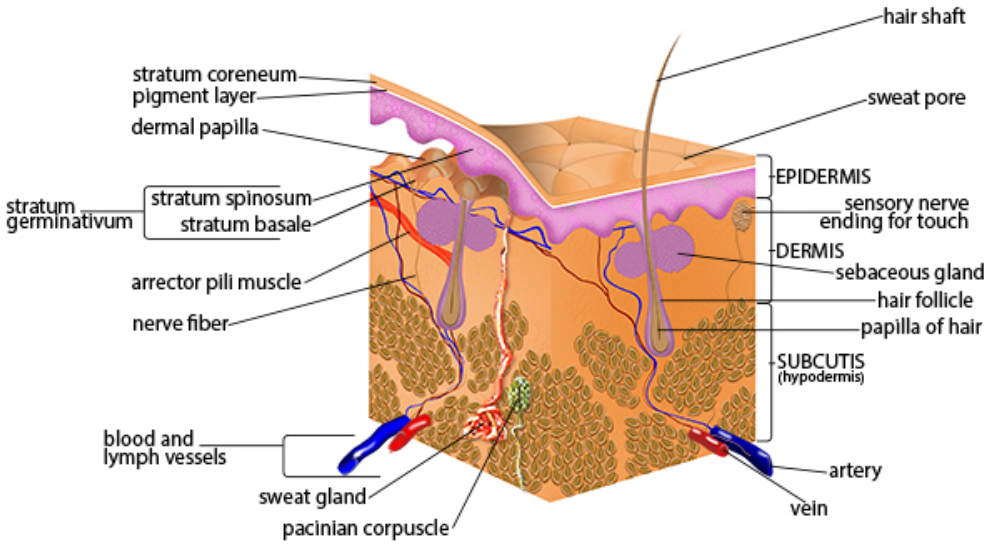

Figure 1: Anatomy of Skin (National Cancer Institute, 2018)

The epidermis is the outer layer of the skin. The deepest layer of the epidermis is known as the stratum basale or stratum germinativum. Here germinative basal cells continuously divide to produce new skin cells. This layer also contains melanocytes that produce melanin to protect the skin from ultraviolet light. Mitotically inactive squamous skin cells proliferate upwards from the stratum

basale into the stratum spinosum. These skin cells produce keratin, the protein that is the major structural component of skin. At the stratum granulosum and stratum lucidum the squamous cells begin to dehydrate and adhere together, forming a durable structure. The outer most layer of the epidermis is the stratum corneum which is entirely made up of dead skin cells (Droual, 2020).

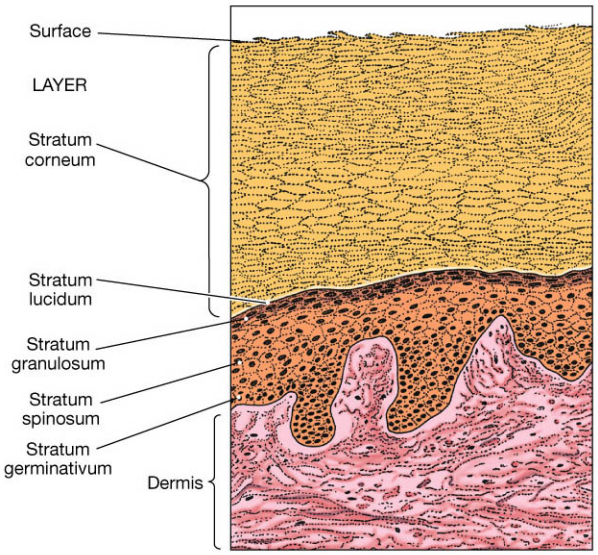

Figure 2: Layers of Epidermis (Droual, 2020)

2.2 Radiation Induced Cancer

The principle concern of occupational radiation exposure is carcinogenesis in mitotically active cells. Deoxyribonucleic acid (DNA) carries the genetic blueprint for cellular function. Unchecked damage to DNA may lead to the proliferation of genetically mutated cells that can disrupt normal biological function, otherwise known as cancer. This is a stochastic process and the probability of occurrence increases with the effective radiation dose received.

The atoms within a strand of DNA may be ionized, breaking bonds between nucleotides. Additionally, radiation may ionize other cellular molecules, forming

highly reactive free radicals (atoms or molecules with an unpaired orbital electron). These free radicals can then diffuse a short distance and scavenge electrons from a strand of DNA. This process is known as indirect action and commonly occurs with H_2O (cells are nearly 80% water).

How radiation interacts with tissue depends on its type, energy, and the elemental composition of the medium. Charged particles (electrons, protons, alphas, etc.) are commonly referred to as directly ionizing. As they traverse through a medium, they disrupt its atomic structure through Coulombic interactions. Electromagnetic radiation (X rays and gamma rays) does not induce biological damage directly due to its neutral charge. However, electromagnetic quanta transfer energy to atomic electrons through a variety of interaction mechanisms depending on incident energy and elemental composition of the target.

Like photons, neutrons are indirectly ionizing. However, rather than interact with atomic orbitals, they transfer energy by physical collision with the nucleus of an atom. Energy transfer depends on the characteristics of the target nucleus and the energy of the incident neutron (Hall & Amato, 2012).

2.3 Neutron Interactions

2.3.1 Scatter

In tissue, there are three interaction mechanisms available to neutrons. The most prevalent interaction at high incident neutron energies (keV-MeV) is scattering. In this process, an incident neutron with kinetic energy, E, collides with a target nucleus of mass A and recoils at some angle with respect to the incident direction of the neutron. If the energy imparted to the recoil nucleus does not result

in an excited state, the scatter is said to be elastic and the average energy transferred is given by:

$$\epsilon_{elastic}^{scatter} = \frac{2EA}{(A+1)^2}\big(1 - f_1(E)\big) \tag{1}$$

Scattering processes have an angular dependence which is defined by the function $f_1(E)$. This is the average cosine of the angle of scatter for a specific incident neutron energy in the center-of-mass system. For the purposes of dosimetry, isotropic scatter is assumed. The average angle of scatter in the center-of-mass system is therefore 90^0 and $f_1(E) = 0$, dropping the term from scattering equations. Other research has utilized both first-order and third-order Legendre expansions, however, no obvious change in depth-dose distributions were observed ((B) Chen & Chilton, 1979).

Unlike elastic scatter, inelastic scatter is a threshold reaction, requiring the incident neutron to carry at least the threshold energy required to excite the recoil nucleus to a specific excited state. This threshold energy is governed by $\Delta = \frac{Q(A+1)}{AE}$, where Q is the amount of energy by which the recoil nucleus is excited above the ground state. As such, the average energy transferred to the recoil nucleus is governed by (Shultis & Faw, 2000):

$$\epsilon_{inelastic}^{scatter} = \frac{2EA}{(A+1)^2}\left(1 + \frac{1}{2}\Delta - f_1(E)\sqrt{1-\Delta}\right) \tag{2}$$

2.3.2 Radiative Capture

In the thermal energy range, radiative neutron capture is prevalent. In this reaction, a target nucleus of mass A absorbs an incident neutron with kinetic energy,

E, and briefly forms a compound nucleus, A'. This atom then emits one or more gamma rays, the characteristics of which are dependent on the nuclide. For instance, the thermal capture by a hydrogen nucleus results in the single emission of a 2.3 MeV gamma ray. Other nuclides may emit an array of gamma rays due to cascades between various nuclear energy levels.

Some photon energy, E_γ, is carried away from the interaction site, depositing energy elsewhere or leaving the tissue medium all together. For whole body dosimetry, some fraction of this energy will contribute to dose. This is further discussed in subsequent chapters; however, conservation of momentum dictates a balance between the energy transferred to the photon and that of the nucleus. As such, the energy transferred to the recoil nucleus is given by (Ritts, 1968):

$$\epsilon_{recoil}^{capture} = \frac{E}{A+1} + \frac{\left(E_\gamma + \frac{AE}{A+1}\right)^2}{A'c^2} \tag{3}$$

2.3.3 Transfer Reactions

Finally, several neutron transfer reactions are possible over a wide range of energies. These are predominantly (n,p) or (n,α) reactions that may require a threshold kinetic energy of the neutron to occur. In this reaction, a compound nucleus is briefly formed before the emission of a charged particle. The subsequent nucleus may be left in an excited state and, depending on the characteristics of the reaction and the energy levels of the nucleus, will emit some number of gamma rays. If a gamma ray is emitted, the energy transferred to charged particles is (Caswell, Coyne, & Randolph, 1980):

$$\epsilon_{transfer} = E_n + Q - E_s \quad (4)$$

Where E_n is the incident energy of the neutron, Q is the energy released in the reaction, and E_s is the excited level that the nucleus enters, often given to a gamma. In the case that no gamma rays are emitted, $E_s = 0$ and all energy released is shared between the emission and the nucleus. A common transfer reaction pertinent to neutron dosimetry is the ^{14}N (n, p) ^{14}C reaction, with a Q-value of 0.62 MeV (Attix, 1986).

2.3.4 Attenuation

As neutrons impinge on a tissue medium, the total number of neutrons available to interact decreases exponentially with tissue depth. This is due to various interactions within the medium that reduce the intensity of the neutron beam as governed by the Beer-Lambert law:

$$\Phi(d, E) = \Phi(d)e^{-\Sigma_t d} \quad (5)$$

where $\Phi(E)$ and $\Phi(d, E)$ are the neutron energy fluence before and after traversing through a medium of thickness (or depth) d, respectively. The total macroscopic cross section describes the probability of any interaction within that medium and can be found through (Attix, 1986):

$$\Sigma_t(cm^{-1}) = \sum_i \left(N_i\sigma_{elastic} + N_i\sigma_{inelastic} + N_i\sigma_{\text{capture}} + N_i\sigma_{transfer}\right) \quad (6)$$

where N_i is the atomic density for a specific element in the tissue medium and σ represents the microscopic cross section for the reaction of concern. The average distance travelled in the tissue medium before an interaction occurs is described as

the mean free path. This value is simply the inverse of the macroscopic cross section and is depicted for tissue as (Shultis & Faw, 2000):

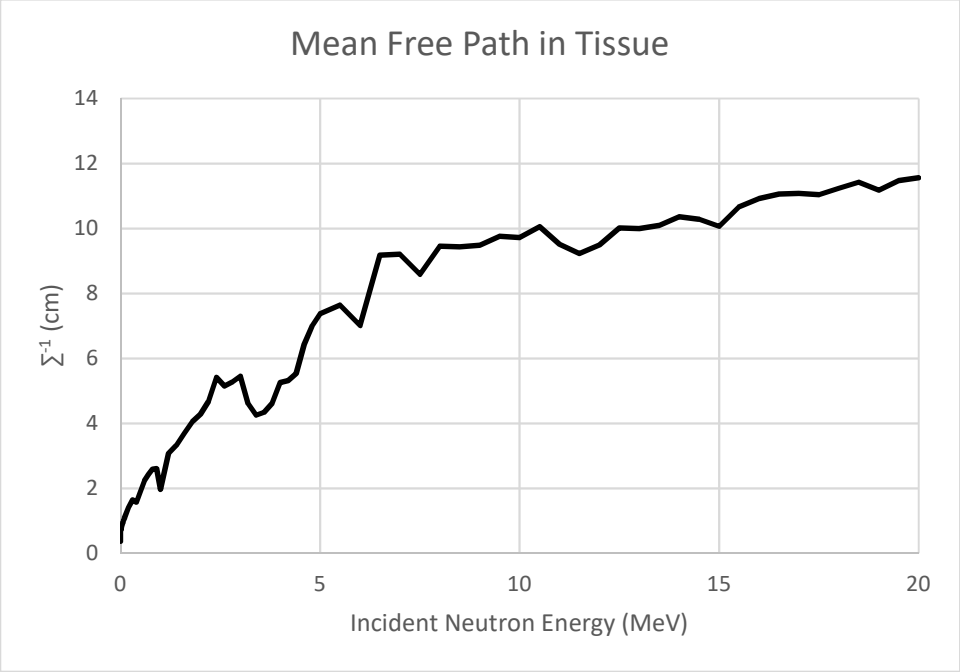

Figure 3: Tissue Mean Free Path

In an infinitely large medium, neutron scatter will eventually slow the neutron to a thermal energy. However, for the sake of dosimetry in small critical volumes, such as the shallow dose region, only a single neutron scattering event is calculated. Even at thermal neutron energies, the mean free path is nearly 0.5 cm, many orders of magnitude larger than the 5 – 10-micron thick segments appropriate to calculate shallow dose.

2.4 Neutron Dose

Neutron KERMA represents the kinetic energy transferred from neutrons to charged particles in an absorbing medium. Since neutrons interact directly with the nucleus, these charged particles are overwhelmingly heavy charged particles. It is

certainly possible for auger electrons to accompany the deexcitation of nuclei following nuclear interactions, however, their contribution is relatively inconsequential. The type and abundance of a reaction that can occur depends on the incident neutron energy, elemental composition of tissue, and the reaction's cross section:

$$K(d,E) = k\sum_j N_j \sum_i \epsilon_{ij}(E)\sigma_{ij}(E)\Phi(\mathrm{d,E}) \tag{7}$$

where k is the energy conversion factor $1.6022x10^{-13}\,\frac{J}{Mev}$, $\epsilon_{ij}(E)$ is the energy transferred to charged particles as kinetic from a specific energy neutron with units of MeV, and $\sigma_{ij}(E)$ is the microscopic cross section for nuclide j and interaction i. The number of atoms per unit mass of element j is represented by N_j and is defined by the ICRU 44 elemental composition of soft tissue (McConn Jr, Gesh, Pagh, Rucker, & Williams III, 2011):

Element	***Mass Fraction (%)***	***N_j (atoms kg^{-1})***
Hydrogen	10.12	$6.093x10^{25}$
Carbon	11.10	$5.57x10^{24}$
Nitrogen	2.60	$1.118x10^{24}$
Oxygen	76.18	$2.867x10^{25}$

Table 1: ICRU Four Component Tissue

It is not that other elements (potassium, calcium, phosphorous, etc.) do not exist in tissue. It is that the total abundance of these elements is negligible relative to the abundance of the four components listed above. It has been shown that an eleven-element tissue model is in excellent agreement with the four-component

simplification. As such, detailed analysis of nuclear reactions that are highly improbable due to their cross section and the relative abundance of a minuscule element are excluded (Caswell & Coyne, 1972).

Unlike KERMA, absorbed dose requires consideration of energy transferred specifically to ionization by secondary charged particles within the dose volume. However, these two values are closely related such that determination of KERMA can be used to approximate dose.

Neutron KERMA is equivalent to dose where charged particle equilibrium (CPE) is established (see Fig 4). In small incremental volumes of tissue, CPE is said to exist if every charged particle leaving the volume is replaced by a charged particle entering with the same energy. Prior to this, at shallower depths in tissue, charged particle equilibrium does not occur. This region is known as the buildup region, where each subsequent volume of interest approaches equilibrium (Attix, 1986).

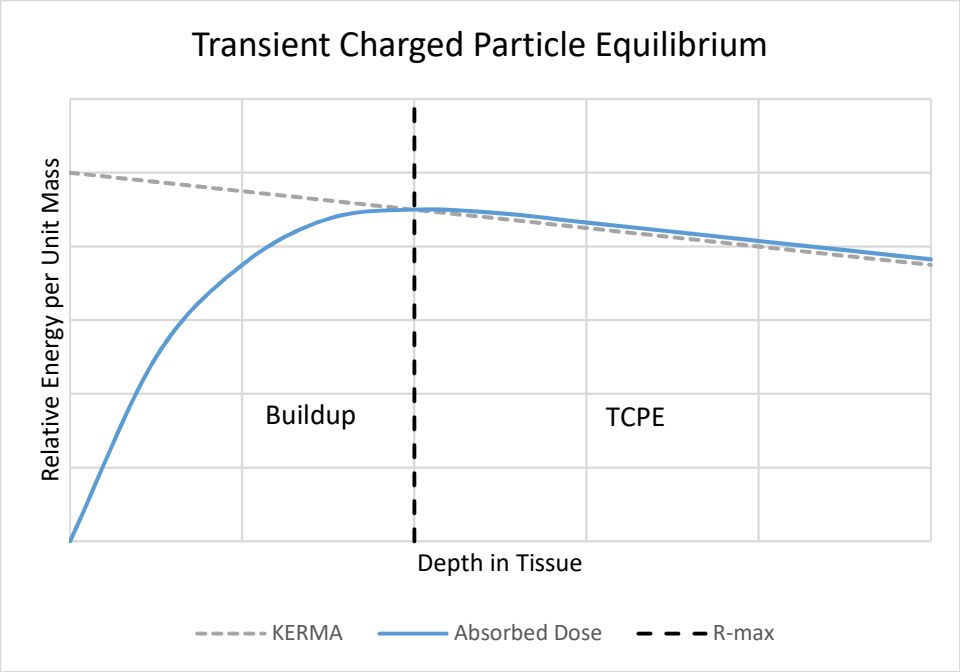

Figure 4:Transient Charged Particle Equilibrium

Dose is equivalent to KERMA at the depth in the medium where CPE is established. When attenuation in a medium is considered, this is known as transient charged particle equilibrium. Essentially, absorbed dose is equivalent to KERMA, however, the number of neutrons interacting with the medium decreases with each subsequent step in the medium due to attenuation. For neutrons incident on tissue, the primary contributor to KERMA is elastically scattered hydrogen due to its large cross section and relatively high abundance. An elastically scattered hydrogen nucleus (proton) can have a maximum energy equivalent to the incident energy of a neutron. As such, CPE occurs at the maximum range of a proton in tissue (see Fig. 5) with kinetic energy equivalent to the incident neutron energy ((A) Chen & Chilton, 1979).

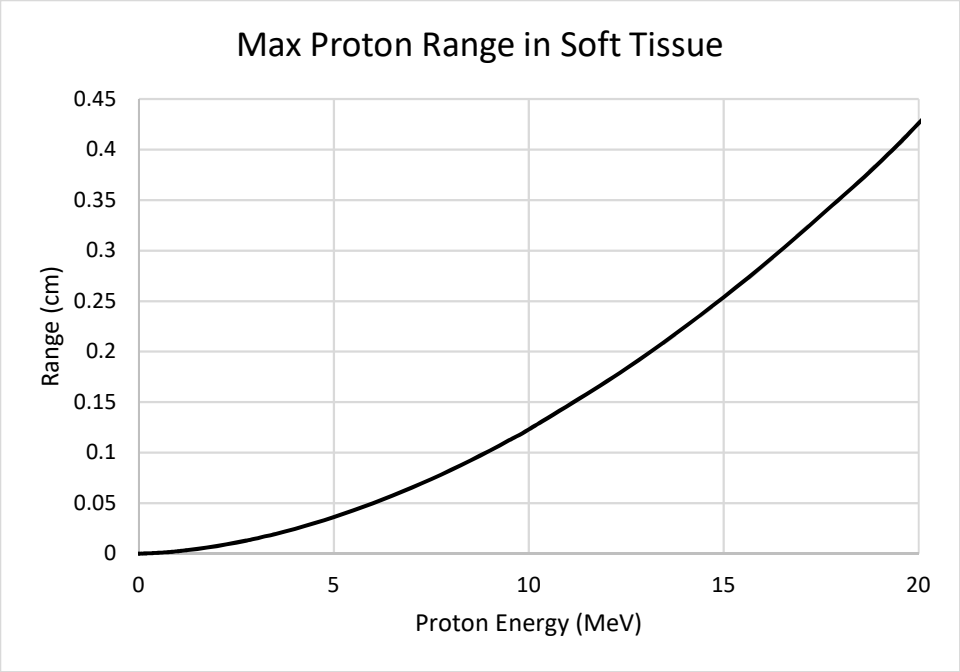

Figure 5: PSTAR CSDA Range in Tissue (National Institute of Standards and Technology, 2019)

Many estimates of dose are carried out assuming CPE exists for all incident neutron energies. However, this is inaccurate for critical skin depths such as that necessary to estimate the shallow dose. For incident neutron energies greater than 2 MeV, the maximum range of the recoil proton exceeds the 0.007 cm depth at which shallow dose is determined. As such, absorbed dose is only a fraction of KERMA at that depth and the assumption does not hold.

2.5 Radiative Whole-Body Photon Dose

Whenever a nucleus enters an excited state, it has a high probability of emitting gamma rays to return to its ground state. In radiative capture, inelastic scatter, and transfer reactions, gamma rays are produced and will ultimately impart energy. However, unlike charged particles, they may travel significant distances before interacting with the medium or leave it entirely.

For small critical volumes, such as that where the shallow dose estimates are made, generated photons have a very small interaction probability. For larger volumes, such as the whole body, the interaction probability increases necessitating the determination of photon dose. This is especially important for thermal neutrons where the $H^1\ (n,\ \gamma)\ H^2$ capture reaction prevails.

Concepts employed in internal dosimetry can be adopted to approximate photon dose. Since neutron interactions within a body are a probabilistic occurrence, the production of photons is randomly distributed throughout the entire body. This is like a homogenously distributed radionuclide that emits photons during radioactive decay. In this case, the number of photons per unit mass of a neutron-generated distributed gamma emitter is given by:

$$Y\left[\frac{Photons}{kg}\right] = \Phi N_j \sigma_{ij} \tag{8}$$

where Φ is the neutron fluence, N_j is the number of atoms per unit mass of a specific constituent, and σ_{ij} is the cross section of that specific reaction leading to the production of photons. Which is related to dose by:

$$D_\gamma = Y F_a E_\gamma k \tag{9}$$

where F_a is the absorbed fraction to the whole body from a specific photon, E_γ is that photon's energy in MeV, and k is an energy conversion factor of $1.6022x10^{-13}\,\frac{J}{MeV}$. Summing over all photon production reactions yields the total whole-body photon dose (Cember & Johnson, 2009).

ICRP 23 appendix I reports a series of Monte-Carlo tests that determined the fraction of energy absorbed by a target organ from a photon of a specific energy emitted in a source organ. The whole-body absorbed fraction, as a function of photon energy, from a homogenously distributed whole-body source is depicted in Fig 6 (International Commission on Radiological Protection, 1974):

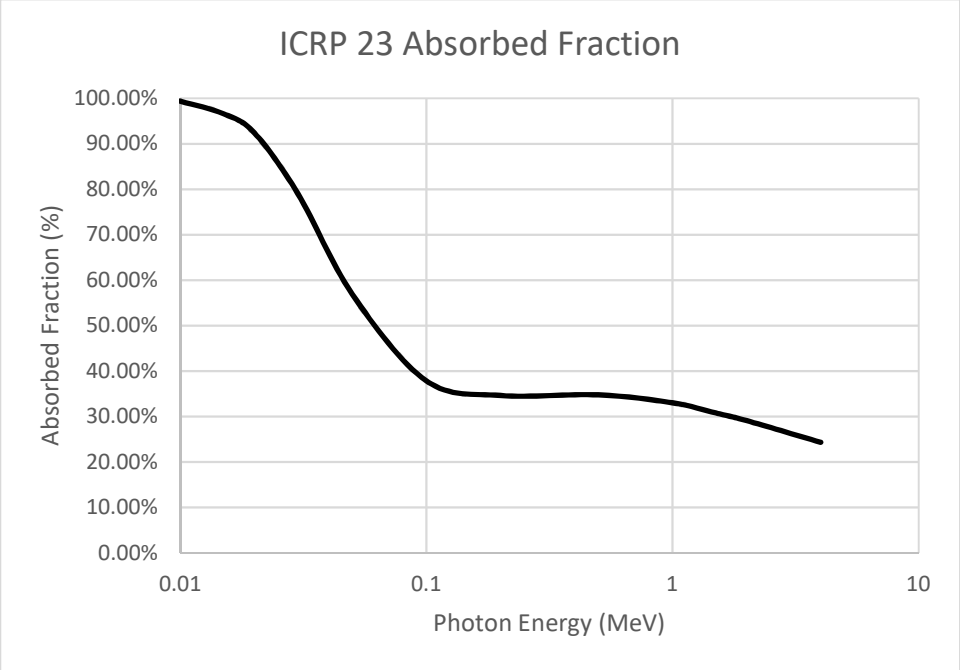

Figure 6: ICRP 23 Photon Absorbed Fraction

2.6 Radiation Weighting Factor

The radiation weighting factor allows one to relate absorbed dose (in units of Gray or rad) to the equivalent dose (in units of Sieverts or rem). While this quantity is derived from absorbed dose, it takes into consideration the biological effectiveness of a specific type of radiation such that the equivalent dose is related to the absorbed dose via:

$$H_T = \sum_R W_R * D_{T,R} \tag{10}$$

where H_T is the equivalent dose, $D_{T,R}$ is the absorbed dose to tissue type T from radiation type R, and W_R is the radiation weighting factor. The radiation weighting factor is based on another quantity, the relative biological effectiveness. This considers the extent of biological damage from a specific type of radiation and compares it to a baseline radiation (Hall & Amato, 2012):

$$RBE = \frac{D_X}{D_R} \tag{11}$$

Various regulatory bodies have concluded that the baseline radiation, D_X, is that of 250 kVp X rays (for medical comparisons). As such, the above term compares the absorbed dose from a specific type of radiation to that of a 250 kVp X-ray spectrum that brings about the same quantity of biological damage. The current recommendation for neutron weighting factors by the ICRP is a continuous function of neutron energy and is depicted by Fig 7 (International Commission on Radiological Protection, 2007):

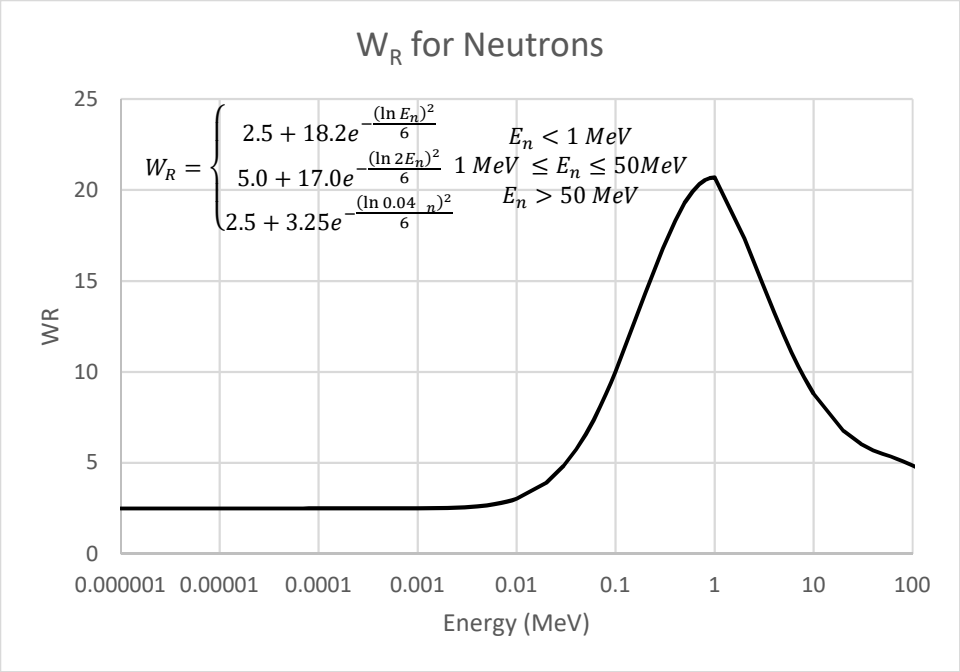

Figure 7: Radiation Weighting Factor for Neutrons

As such, a 1 MeV neutron produces nearly twenty times the biological damage as 250 kVp X rays. Unlike neutrons, photons have a radiation weighting factor of unity (1) at all energies.

3 Materials and Methods

3.1 Cross Sectional Data

A complete set of pertinent nuclear reaction cross sections is imperative to neutron dosimetry. These cross sections are under constant revision as computational/experimental capability continues to improve. The methods and resources utilized in the selection of cross sections pertinent to neutron dosimetry are described here.

3.1.1 The Evaluated Nuclear Data File

In the previous chapter, a series of equations were discussed to derive the energy transferred to charged particles from neutron interactions. However, to accurately calculate KERMA over a range of neutron energies, accurate cross-sectional data for each constituent in a tissue medium must be utilized.

There exists the Evaluated Nuclear Data File which maintains current experimental nuclear data in a library format. It contains data such as cross sections, spectra, angular distributions, etc. with emphasis on neutron induced reactions. This database is an international collaboration hosted by the International Atomic Energy Agency and frequently updated with experimental data derived from regional and national libraries (USA, Europe, Japan, Russia, and China). As such, it is a comprehensive source of the most up-to-date cross-sectional data pertaining to nuclear reactions (International Atomic Energy Agency, 2020).

3.1.2 Pertinent Cross Sections

Cross sections were selected based on overall contribution to KERMA. For example, within the lower neutron energy range (thermal to keV) radiative capture is the dominant reaction for all constituent nuclei except nitrogen, where the (n, p) reaction is many orders of magnitude more probable. At intermediate energies (keV-MeV) elastic scatter with all constituent nuclei is the eminent reaction. In fact, due to its high probability and relative atomic density, KERMA due to the elastic scatter of hydrogen is nearly equivalent to total KERMA (International Atomic Energy Agency, 2020).

Table 2 lists the nuclear reactions that are considered within this report. They are broken down by each constituent with increasing atomic number. If there are photons associated with the reaction, they are ranked by decreasing energy. For threshold reactions where several photons may occur, their excited level is listed in the fourth column. Finally, the Q-value for reactions is also included. Those with positive Q-values spontaneously occur while those with negative Q-values are known as threshold reactions, requiring that amount of input energy to occur.

Nuclear Reaction	**Photon Energy (MeV)**	**Reaction Q-Values (MeV)**	**Excited Level Associated with Photon (MeV)**	**Database Source**
H (n, n) H	-	-	-	ENDF/B-VIII.0
H (n, γ) H	2.225	2.225	-	ENDF/B-VIII.0
C (n, n) C	-	-	-	ENDF/B-VIII.0
C (n, n') C	γ_1: 4.813	-4.813	4.813	ENDF/B-VII.1
C (n, γ) C	4.946	4.946	-	ENDF/B-VIII.0
C (n, α) Be	-	-5.702	-	ENDF/B-VIII.0
C (n, n')3α	-	-7.275	-	CENDL-3.1
N (n, n) N	-	-	-	ENDF/B-VIII.0
N (n, n') N	γ_1: 7.029	-2.313	7.029	ENDF/B-VIII.0
	γ_2: 5.106		5.106	
	γ_3: 2.313		2.313	
	γ_4: 1.635		3.948	
	γ_5: 0.728		5.834	
N (n, γ) N	10.833	10.833		ENDF/B-VIII.0
N (n, p) C	-	0.626	-	ENDF/B-VIII.0
N (n, d) C	-	-5.326	-	ENDF/B-VI
N (n, t) C	-	-4.015	-	ENDF/B-VI
	γ_1: 4.439		4.439	ENDF/B-VIII.0
N (n, α) B	-	-0.158	-	JENDL-3.3
	γ_1: 5.020		5.020	ENDF/B-VIII.0
	γ_2: 4.445		4.445	ENDF/B-VIII.0
	γ_3: 2.125		2.125	ENDF/B-VIII.0
N (n, 2α) Li	-	-8.822	-	ENDF/B-VIII.0
O (n, n) O	-	-	-	ENDF/B-VIII.0
O (n, n') O	γ_1: 7.117	-6.049	7.117	ENDF/B-VIII.0
	γ_2: 6.917		6.917	
	γ_3: 6.130		6.130	
	γ_4: 2.742		8.872	
O (n, γ) O	4.143	4.143	-	ENDF/B-VIII.0
O (n, p) N	-	-9.637	-	ENDF/B-VI
	γ_1: 0.297		0.297	ENDF/B-VIII.0
	γ_2: 0.277		0.398	ENDF/B-VIII.0
	γ_3: 0.120		0.120	ENDF/B-VIII.0
O (n, d) N	-	-9.903	-	ENDF/B-VI

	$\gamma_{1:}$ 5.299		5.299	ENDF/B-VIII.0
	$\gamma_{2:}$ 5.270		5.270	ENDF/B-VIII.0
O (n, α) C	-	-2.214	-	ENDF/B-VI
	γ_1: 3.854		3.854	ENDF/B-VIII.0
	γ_2: 3.686		3.686	ENDF/B-VIII.0
	$\gamma_{3:}$ 3.089		3.089	ENDF/B-VIII.0
	$\gamma_{4:}$ 0.169		3.854	ENDF/B-VIII.0
O (n, n`α) C	4.438		4.438	ENDF/B-VIII.0

Table 2: Evaluated Nuclear Reactions in Tissue

The reactions discussed in the previous paragraph constitute those that have some probability of occurrence over the entire energy range. Other reactions, such as inelastic scatter and transfer, have an associated threshold energy typically on the order of several MeV. The excited states of subsequent compound nuclei for reactions with carbon, nitrogen, and oxygen are reached with increasing likelihood as the energy of the incident neutron approaches 20 MeV. Such reactions do not always result in the simple emission of a single particle; an array of photons may be emitted according to the excited state that the compound nucleus enters.

For many reactions, especially inelastic scatter and (n, α), there exist many excited states that the compound nucleus may enter. For instance, the ENDF/B-VIII.0 includes 43 cross sections each associated with the emission of a different photon resulting from inelastic scatter with nitrogen. However, most of these cross sections are many orders of magnitude less than the most significant cross section. As such, the only cross sections included in the report are those that are on the same order of magnitude as the largest cross section for a specific reaction.

3.2 Software and Computing

3.2.1 MCNP

All depth-dose simulations were performed with Monte Carlo N-Particle (MCNP). This is a general-purpose code maintained by Los Alamos National

Laboratory and used for neutron, photon, electron, or coupled radiation transport simulations, including secondary gamma rays generated through neutron interactions. The latest version, MCNP6.2, has combined the physics models employed by MCNP5 and MCNPX allowing for more accurate charged particle transport. As such, MCNP6 can produce and track the light ions created by elastic scatter of light nuclei (protons, deuterium, tritium, alphas, etc.). Proper two body kinematics are utilized to track these recoil particles by energy and scatter angle (Zieb, Hughes, James, & Xu, 2018).

User's generate an input file that describes what is to be simulated through a series of "cards". The *surface card* is utilized to define where on a cartesian coordinate system specific surfaces exist. These surfaces have several predefined geometries (plane, disk, cylinder, etc.) and are used to bound volumes. These volumes, i.e. "cells", are created on the cell card with respect to user defined surfaces. For instance, if a cylindrical surface is created and the user wishes to define the inside of the cylinder as a cell, that cell is "negative" to the surface of the cylinder and all space outside of it is "positive". Finally, the *data card* allows the user to define material composition, location of tallies, radiation sources and their specifications (Shultis & Faw, 2011).

MCNP will execute the input file and perform a series of statistical tests on the output. The output is determined by user specification within the input file. The primary use of MCNP for the present study is to determine the relationship between neutron KERMA and dose at specific depths in tissue. As such, the output is a series of values associated with each tally and cell of concern.

3.2.2 TableCurve2D

TableCurve2D is a linear and non-linear automated curve fitting software. It is used to fit and rank a variety of equations to data provided by the user. Once ranked, the user may evaluate and choose an equation that best represents that data. For the purpose of this study, the data to be evaluated is the ratio between absorbed dose and KERMA (Systat Software, 2020).

For a wide range of energies, MCNP output is translated into a TableCurve2D readable file and imported into the software. A single equation is chosen that best fits the data at each energy. The coefficients of this equation change with energy, thus requiring a similar process to develop equations describing each coefficient. Depending on the physical phenomena being modelled, a series of equations with different domains may be used to accurately reflect the originally simulated data.

3.2.3 Computational Specifications

The computational specifications used in this study were 16 GB of RAM and an Intel Core i5-8250U four-core processor rated at 1.6 GHz per core. While MCNP6 allows the user to select the number of cores used per simulation for most transport problems, that is not a possibility for non-analog neutron transport. Any further improvement in processing speed would drastically increase the history rate of the simulation.

3.3 Simulation Materials and Geometry

For the evaluation of fractional charged particle equilibrium, a model reflective of a true skin target was developed. MCNP requires explicit material and

geometric definitions to accurately evaluate the physics transport question at hand. As such, the methods to evaluate absorbed dose and KERMA with depth are described here.

3.3.1 Skin Composition

The material composition of skin used for Monte Carlo simulation is consistent with that used in past studies. This corresponds to the four-component tissue defined by the ICRU and previously discussed in Chapter 1. Within MCNP the designation of material composition is as follows (McConn Jr, Gesh, Pagh, Rucker, & Williams III, 2011).

```
c ICRU 4 COMPONENT SOFT TISSUE MATERIAL DEFINITION **********************
m1    1001 -0.101172
      6000 -0.111000
      7014 -0.026000
      8016 -0.761828
```

Figure 8: Material Card Format for MCNP

The first material in the input file (the only material in this simulation) is identified as M1. For neutron transport problems, a specific isotope of an element must be specified with its ZAID number. The ZAID number takes on the format ZZZAAA, where Z and A are the element's atomic number and atomic mass number, respectively. If the material does not have a corresponding atomic mass number, such as carbon in this case, MCNP assumes its natural distribution. Currently data tables for the 6012 designation do not exist, however, the natural abundance of carbon-12 is relatively high (~99%) such that utilizing the 6000 designator has little impact on the simulation. The negative values correspond to the mass fraction of each element in the constituent material (Los Alamos National Laboratory, 2017).

3.3.2 Geometry

As previously discussed, each cell must be bound by defined surfaces. These surfaces are placed on a cartesian coordinate system and designated by geometric mnemonics. Each surface is assigned an arbitrary surface number that is best ordered in a way that is easy to understand to the user.

```
C SURFACE CARDS************
1          py  4
2          py -10
3          cy  10
4          cy  1.78412412
11  py  0
12  py  -0.0005
13  py  -0.0015
14  py  -0.0025
15  py  -0.0035
16  py  -0.0045
17  py  -0.0055
18  py  -0.0065
19  py  -0.0075
20  py  -0.0085
21  py  -0.0095
22  py  -0.0105
```

Figure 9: Surface Card Format for MCNP

The first two surfaces (#1 and #2) define the outer bounds of the simulation. Two infinite planes, perpendicular to the y-axis (PY mnemonics), are placed along the y-axis at 4 and -10 centimeters, respectively. The next two surfaces (#3 and #4) are cylinders parallel to and centered along the y-axis. The first has a radius of 10 centimeters while the second has a radius of 1.78 centimeters, corresponding to a surface area of 10 cm^2. The cylinders are then divided into thinner segments with a series of planes placed 5 – 10 microns apart depending on simulation criteria (surfaces 11 through 1113).

```
C CELL CARDS**********************************
1       0        -1   11   -3   imp:p,e,h,n 1
2       0         2 -1113   -3   imp:p,e,h,n 1
3       0         1:-2:3      imp:p,e,h,n 0
4       1   -1    4   -3   1113   -11       imp:p,e,h,n 1
11   1    -1   -11  12   -4   imp:p,e,h,n 1
12   1    -1   -12  13   -4   imp:p,e,h,n 1
13   1    -1   -13  14   -4   imp:p,e,h,n 1
14   1    -1   -14  15   -4   imp:p,e,h,n 1
15   1    -1   -15  16   -4   imp:p,e,h,n 1
16   1    -1   -16  17   -4   imp:p,e,h,n 1
17   1    -1   -17  18   -4   imp:p,e,h,n 1
18   1    -1   -18  19   -4   imp:p,e,h,n 1
19   1    -1   -19  20   -4   imp:p,e,h,n 1
```

Figure 10: Cell Card Format for MCNP

With the surfaces defined, cells are created to fill all space in the coordinate system. The first cell is negative with respect to plane 1, positive with respect to plane 11, and negative with respect to surface 3 (or inside the largest cylinder). It has a material designator of 0, meaning that the space within it is void and, as such, has no density. The second cell is positive with respect to plane 2, negative with respect to plane 1113, and negative with respect to surface 3. Both cells are designated as important to photons, electrons, protons, and neutrons by the imp: p, e, h, n 1 designator. Unlike the first and second cells, the third cell is known as the graveyard. This defines all space outside of the scope of the simulation and is mandatory for MCNP to run. As such, cell 3 is the union of all space positive with respect to surfaces 1 and 3 and negative with respect to surface 2 which is completely void of material. In addition, it is given no importance to photons, electrons, protons, or neutrons and will kill them if they enter this area during the simulation.

Since this study is concerned with the depth dose of neutrons impinging on a tissue target, specific cells are designed to aid in the simulation of dose and KERMA at equidistant slabs of tissue. Cell 4 consists of material 1, the ICRU four-component soft tissue previously defined, and has a density of 1 g cm^{-3} (designated by the -1 in the third column). This cell is negative with respect to surface 3 and 11 while being positive with respect to surface 4 and 1113. In simpler terms, all material between the smaller and larger cylinders and planes 11 and 13 is tissue for the purpose of physics transport. However, it is not further divided into cells because it is of no importance to the tallying of KERMA and dose. It exists to allow for scatter of radiation back into the critical volume of tissue, a process that would occur in a natural exposure scenario.

Finally, each subsequent cell from 11 through 1112 is negative with respect to surface 4 and the previous cell (negative with respect to surface n and positive with respect to surface n + 1 where n is 11…1112). They all have a material designation of ICRU four-component tissue and a density of 1 g cm^{-3}. Essentially, this divides the small cylinder into a series of tissue segments that are 10 microns in thickness and have a surface area of 10 cm^2 (corresponding to a volume of 0.01 cm^3). A representation of this geometry is depicted in figure 11:

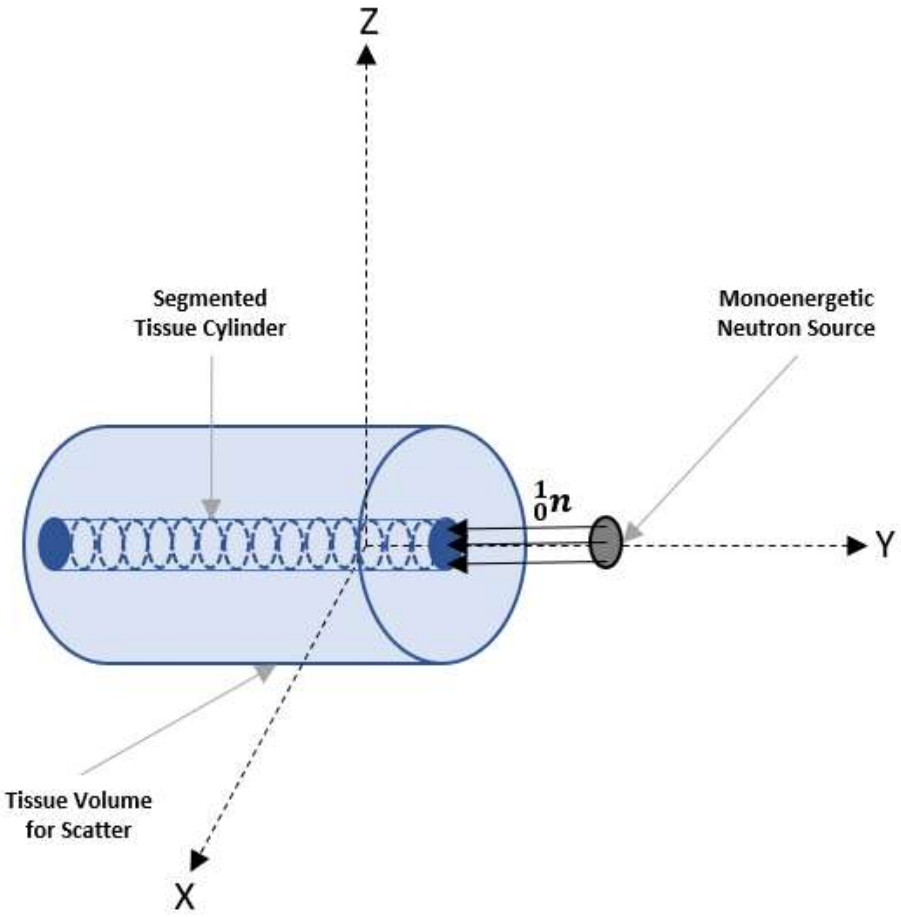

Figure 11: Geometry of MCNP Simulation

3.4 MCNP6 Source Definition

In this study, monoenergetic neutrons (PAR n) are simulated as being emitted from a monodirectional planar source; this simulation is defined on the *SDEF card*. The source is located (POS) in a vacuum two centimeters in front of the segmented tissue cylinder and oriented perpendicular to the y-axis (AXS). Neutron energies (ERG) from thermal to 20 MeV were varied over a series of runs and emitted in the negative y-axis direction (VEC). The source information modifier (SI1) sets the radial sampling range from 0 to 1.784 centimeters, essentially creating a disk source with the same surface area as the segmented tissue cylinder (10 cm^2). In this case,

the source probability modifier (SP1) sets the radial sampling weight to be equivalent along the entire source disk.

```
C SOURCE CARD************************************************************
mode     p e h n
PHYS:N J 100 0 J J J 4
cut:h J 1E-3
sdef     par n erg 17 pos 0 2 0 ext 0 rad d1 axs 0 1 0 vec 0 -1 0 dir 1
si1      0 1.78412412
sp1      -21 1
```

Figure 12: Source Card Format for MCNP

The *mode data card* simply designates all the particles that will be transported and tracked by MCNP. Neutron physics (PHYS:N) specifications are made on the *physics data card*. MCNP will track the recoil of light ions created during elastic scatter utilizing nuclear data tables. In the off chance of neutron capture in a generated lithium of boron atom, the Neutron Capture Ion Algorithm (NCIA) is employed (the value of 4 in the seventh placeholder). However, this is negligible relative to the other reactions occurring in the four-component model since this algorithm is specific only to helium, lithium, and boron neutron capture. The energy cutoff for proton recoil (CUT:H) is lowered to allow for further tracking of lower energy protons. At an energy of 1 keV, proton transport is killed since the range of a proton is significantly less than the cell thickness (Los Alamos National Laboratory, 2017).

3.5 MCNP Tallies

3.5.1 F6:N KERMA Tally

The F6:N tally measures the energy deposition averaged over a cell for neutrons. Energy deposition is determined from the *heating numbers* in the nuclear data tables employed by MCNP. These heating numbers are estimates of the energy

deposited per unit track length per particle type. For accurate energy deposition calculation, possible secondary emissions are included on the MODE card. If a secondary particle is not specified, MCNP assumes local energy deposition i.e. the point of interaction. If there is no tabular data from which MCNP can draw, charged particle ionization energy (dE/dx) is deposited uniformly along the particle's track.

The F6:N tally works by tracking the energy of a neutron before and after leaving a cell volume. The difference in energy is assumed to be deposited in the cell of interest. As such, this tally only tracks the energy transferred to the medium by neutrons and returns the KERMA in units of MeV g^{-1} (Los Alamos National Laboratory, 2017).

3.5.2 +F6 Dose Tally

The +F6 tally is known as the *collision heating tally* and has units in MeV g^{-1}. It has no particle designator as it applies to all particles generated through the course of the simulation. Energy deposition is tracked for each particle averaged over every cell of concern for all types of library interactions possible in MCNP. It employs library heating value data and dE/dx energy information for a variety of particles.

As a result, energy deposited per unit cell volume from all particles is calculated. Unlike the F6:N tally, which primarily considers energy transferred to the medium specifically from neutrons, energy deposition is due to the slowing of charged particles, recoil of nuclei, and energy deposited locally for particles that are born but not tracked. As such, the +F6 tally is used in the calculation of absorbed dose (Los Alamos National Laboratory, 2017).

3.6 Depth-Dose Calculation

With each energy, the ratio of dose to KERMA (+F6/F6:N) with depth is determined. A series of charts are generated and imported into TableCurve2D where a specific function is fit to all curves. The coefficients for this function changes with incident neutron energy, requiring a similar methodology to determine a suitable equation that describes each coefficient. Finally, a single equation is generated with the variables of energy and tissue depth.

3.7 Dose Approximation

Considering the dominant neutron interactions that occur in tissue over the range of thermal to 20 MeV, a set of KERMA values can be generated utilizing the equations discussed in chapter 2. The depth-dose equations described in chapter 3 can then be applied to these values for a more accurate representation of dose at a specific depth. This is especially important in the energy range where charged particle KERMA is not equivalent to dose (1 MeV-20 MeV).

If one wishes to determine whole-body dosimetry, dose contribution from photons is determined as described in chapter 2. Slow neutrons generate a considerable number of secondary photons such that the dose from photons is on a similar order of magnitude as neutrons for whole-body dosimetry. The set of equations that describe this phenomenon is likewise employed over the energy range of concern.

This culminates into a neutron dose model wherein the dose from a monoenergetic neutron at a shallow depth can be determined simply through the input of the neutron's energy, fluence, and tissue depth. Additionally, whole-body

dosimetry can be approximated by accounting for photons. When a distribution of neutron energies and probabilities is applied to the model, such as that of an americium-beryllium source, a dose distribution representative of a real source can be determined.

4 Results and Discussion

4.1 Fractional Charge Particle Equilibrium (f_{CPE})

As described in section 3.6, the ratio between dose and KERMA with tissue depth was simulated with MCNP over the 1 – 20 MeV energy range. Two equations were generated with the resulting data using TableCurve2D and are described herein. Their respective fits are plotted against the MCNP data in Appendix B.

4.1.1 1 – 5 MeV Range

Due to the relatively short range of maximum recoil protons in this energy domain (< 350 microns), tissue segments were simulated at thicknesses of 5 microns. As such, a function was developed and fit to the MCNP results for neutron energies between 1 and 5 MeV:

$$f_{cpe}(E,d) = A + B(10d) + C(10d) * ln(10d) \quad (12)$$

where d is the tissue depth of interest in centimeters and A, B, and C are energy dependent coefficients each described by their respective fits:

$$A = aE^4 + bE^3 + cE^2 + dE + e \quad (13)$$

$$B = a + bE^{0.5} + cE + dE^{1.5} + eE^2 + fE^{2.5} + gE^3 + hE^{3.5} \quad (14)$$

$$C = a + \frac{b}{E^{1.5}} + \frac{c * ln(E)}{E^2} + \frac{d}{E^2} \quad (15)$$

The coefficients a through h are listed below in Table 3:

Coefficients

	A	B	C
a	-0.0011	28750.5170	-2.977
b	0.0085	-129230.7936	233.4216
c	-0.0121	243025.4594	-146.5497
d	-0.0318	-249298.7577	-259.5103

e	.1959	151141.5442	-
f	-	-54262.00968	-
g	-	10695.8419	-
h	-	-893.8685	-

Table 3: Coefficients for fcpe ≤ 5 MeV

4.1.2 5 – 20 MeV Range

For higher energy photons, between 5 and 20 MeV, the maximum recoil range of protons is enough to allow for tissue segmentation of 10 microns. The resulting functional fit to the MCNP data is given as:

$$f_{cpe}(E,d) = A + Bd + Cd^2 + Dd^3 \tag{16}$$

where the tissue depth, d, is given in units of centimeters and A, B, C, and D are energy dependent described by:

$$A = aE^4 + bE^3 + cE^2 + dE + e \tag{17}$$

$$B = a + bE^{1.5} + cE^3 + d * ln(E) \tag{18}$$

$$C = a + bE^2 ln(E) + c * ln(E) + \frac{d}{E^2} \tag{19}$$

$$D = a + \frac{b}{E} + \frac{c}{E^2} + \frac{d}{E^3} \tag{20}$$

The energy of the incident neutron, E, is in units of MeV and the respective coefficients for these equations are found in Table 4:

	Coefficients			
	A	**B**	**C**	**D**
a	-0.000011493	138.80269	799.55938	-174.65853
b	0.00036556	1.16205	0.06663	9376.63316
c	-0.0031751	-0.0040091	-275.78493	-164341.05421
d	0.012203	-69.03516	-24762.65796	1002172.16358
e	0.20591	-	-	-

Table 4: Coefficients for fcpe ≥ 5 MeV

4.1.3 Evaluation of f_{cpe}

As previously discussed, charged particle equilibrium is reached at the maximum recoil range of a proton for a specific incident neutron energy. The National Institute of Standards and Technology maintains the PSTAR database which can be utilized to plot stopping power and range for protons in ICRP tissue as a function of energy. The resultant data has been compared to the set of equations developed for this report (National Institute of Standards and Technology, 2019).

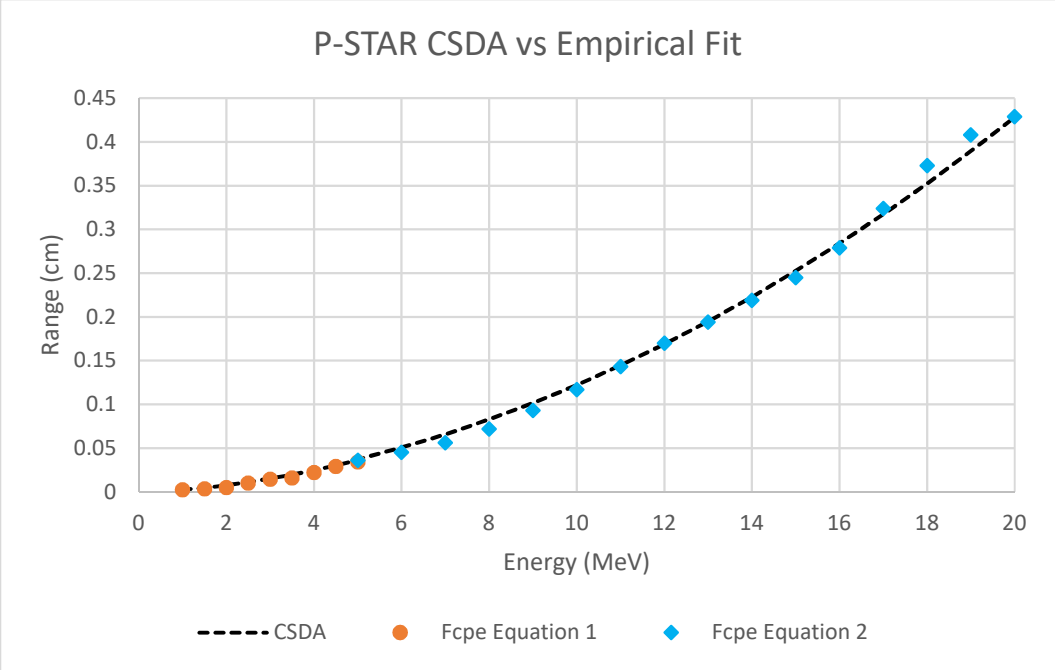

Figure 13: PSTAR vs Evaluated Data

Knowing that charged particle equilibrium is established at the maximum range of elastically scattered hydrogen, for each equation and energy the point at which CPE occurs is compared to PSTAR values. As depicted in Figure 13, both empirically derived equations follow a similar trend to the Continuous Slowing Down Approximation (CSDA) in ICRU tissue. There are slight discrepancies at

several points, however, the equations developed are still reflective of MCNP results as shown in Appendix B.

In addition, a previous study conducted in the late 70's by Chen and Chilton (1979) evaluated the depth-dose relationship of fast neutrons near the skin. They utilized a procedure similar to that in this work, however, due to computational limitations at the time, tissue segments were limited to a thickness of 1 millimeter. For four neutron energies, the percentage of absorbed dose was determined and plotted for penetration depths up to 0.5 centimeters. Their results are compared to the MCNP simulation described in the report ((A) Chen & Chilton, 1979).

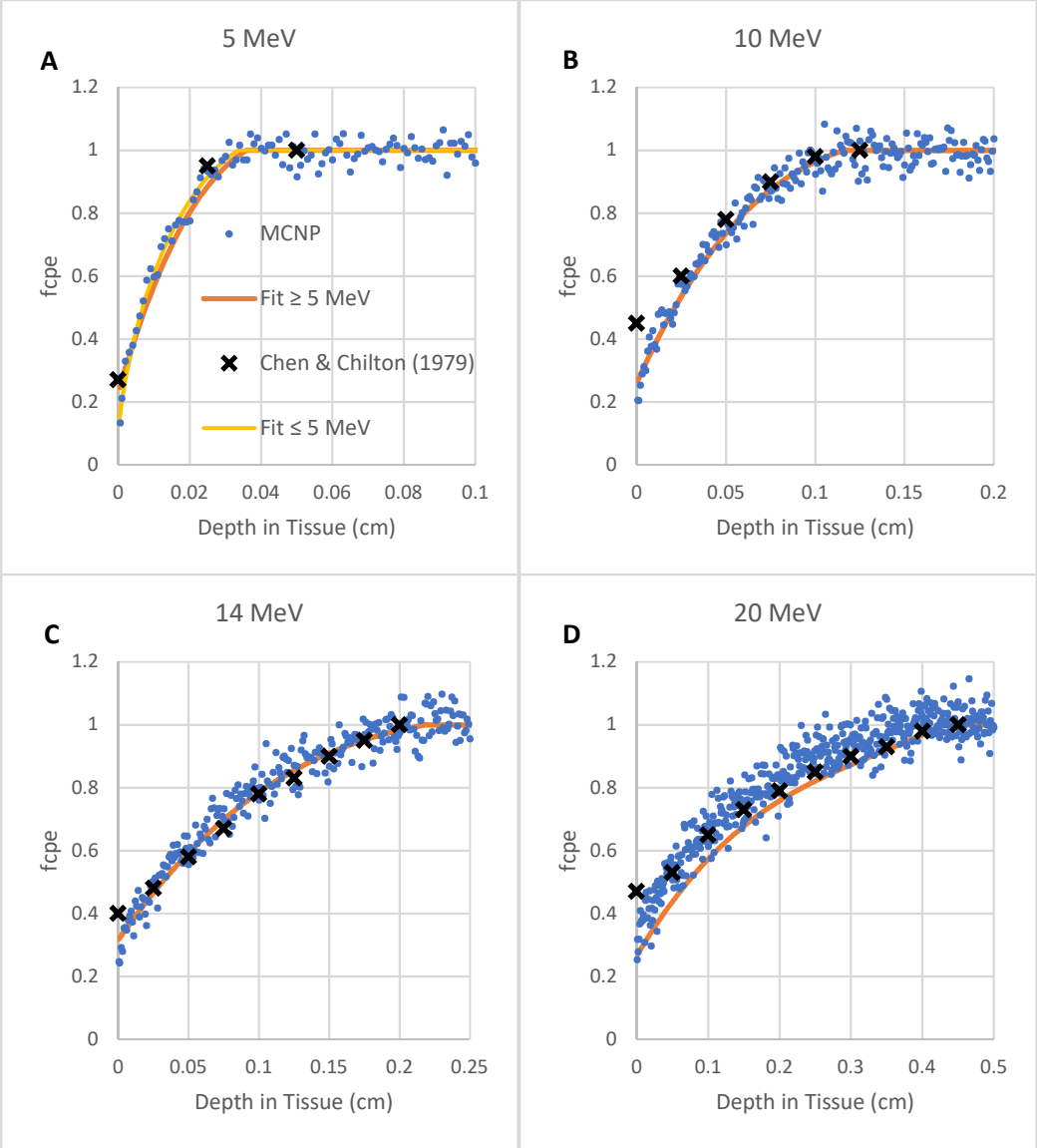

Figure 14: fcpe comparisons (a) 5 MeV (b) 10 MeV (c) 14 MeV (d) 20 MeV

As depicted in Figure 14, the two sets of equations are good fits for the MCNP data collected. Additionally, values pulled from Chen & Chilton demonstrate further confirmation of both the MCNP and TableCurve2D functional fits. A noticeable discrepancy occurs at very small shallow depths where f_{cpe} calculated by Chen & Chilton is nearly twice that of what was calculated in this report.

These differences are due to the different tissue segment thicknesses simulated. Significant computational improvements since 1979 allows for reasonable simulation of tissue segments in the micron range. At the time Chen & Chilton conducted their investigation, this was not a possibility. They were limited to 1-millimeter segments which allows for additional energy absorption from charged particles, thus increasing the absorbed fraction ((A) Chen & Chilton, 1979).

4.2 Neutron KERMA

4.2.1 Constructed KERMA for Tissue Constituents

As discussed in Section 3.1, pertinent cross sections were pulled from the Evaluated Nuclear Data File to build neutron KERMA in tissue. These cross sections were utilized in conjunction with the equations discussed in Sections 2.3 and 2.4. Each reaction was evaluated individually before summation to determine the total KERMA at a given incident neutron energy (Figure 15):

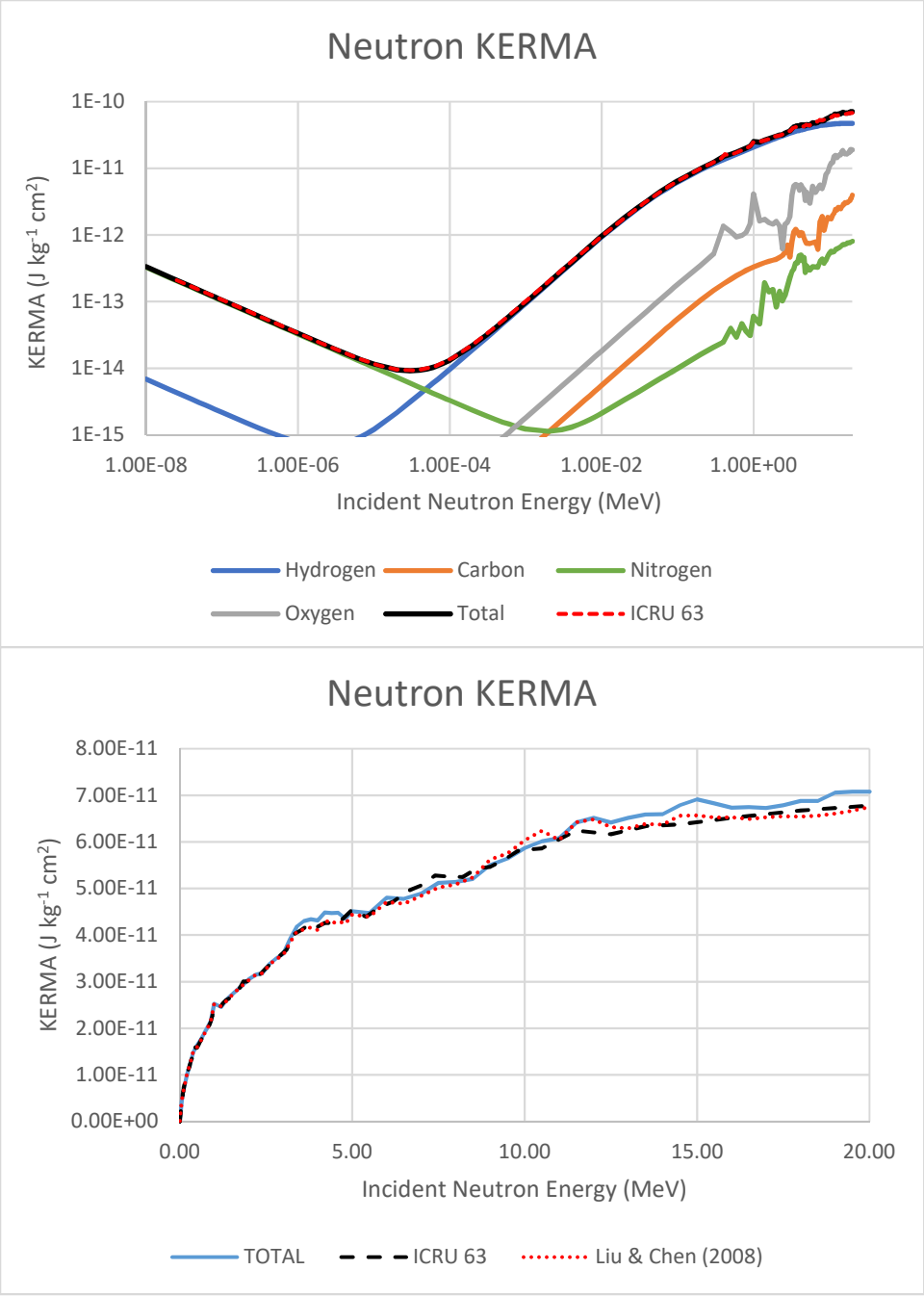

Figure 15: ICRU KERMA vs Evaluated Data (a) Logarithmic (b) Linear

The evaluated data compares well with the International Commission on Radiation Units and Measurements values. However, there are variations in the higher MeV range primarily due to the modelling of threshold reactions in oxygen, nitrogen, and carbon. A previous study conducted by Liu and Chen (2008)

evaluated the constituent KERMA extensively and reported a new set of values. Their results are compared to the evaluated data from this report and ICRU recommendations in Figure 16 (International Commission on Radiation Units and Measurements, 2000), (Liu & Chen, 2008):

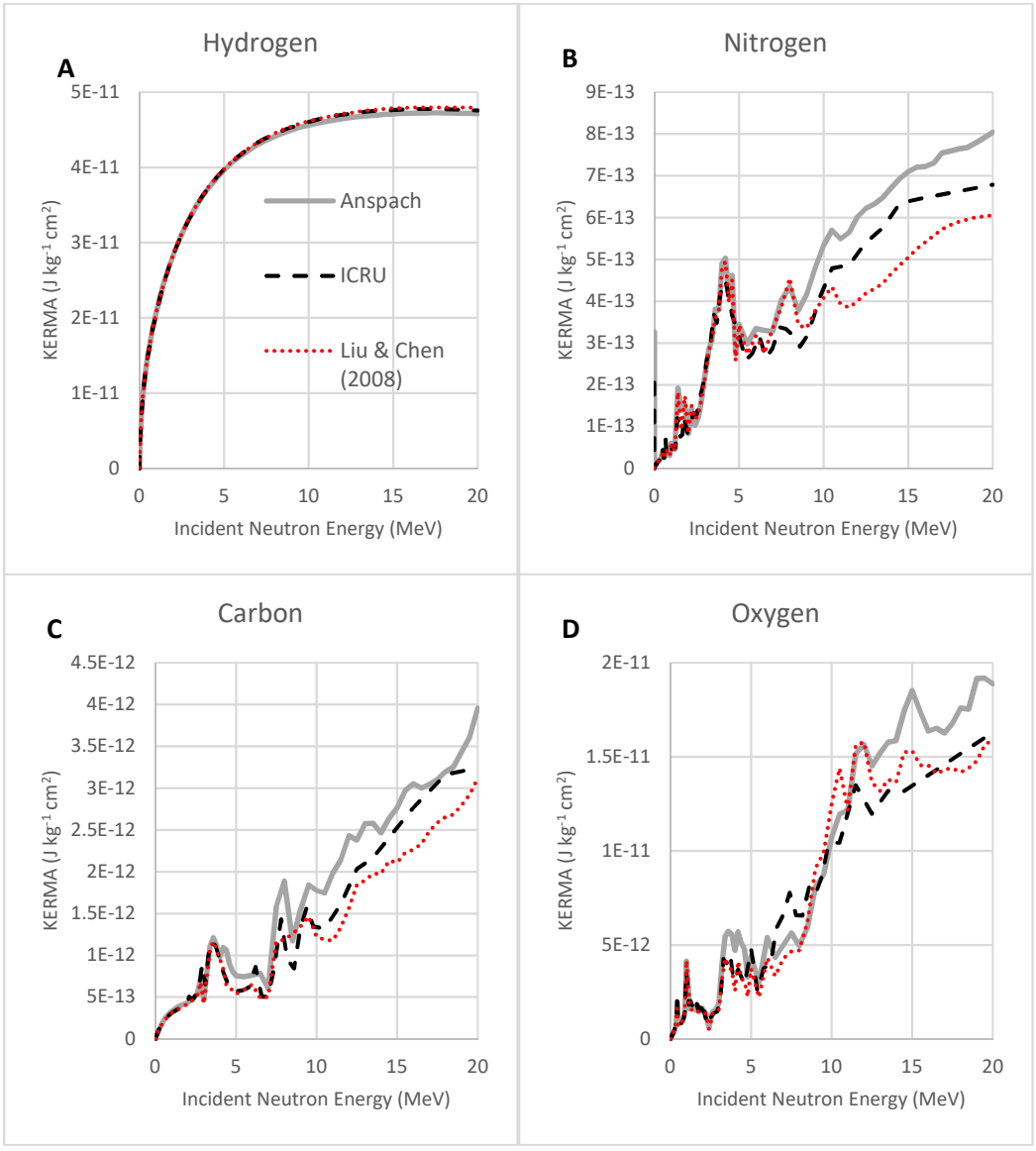

Figure 16: Constituent KERMA Comparisons (a) Hydrogen (b) Nitrogen (c) Carbon (d) Oxygen

4.2.2 Evaluation of KERMA

Using ICRU 63 (2000) for comparison, the percent difference for the reported KERMA values is determined over the entire energy range modelled. This

is represented by Figure 17 where, generally, there are three ranges with noticeable variation in their trends. This includes the energy ranges of 0.01 eV – 10 eV, 10 eV – 10 keV, and 10 keV – 20 MeV (International Commission on Radiation Units and Measurements, 2000).

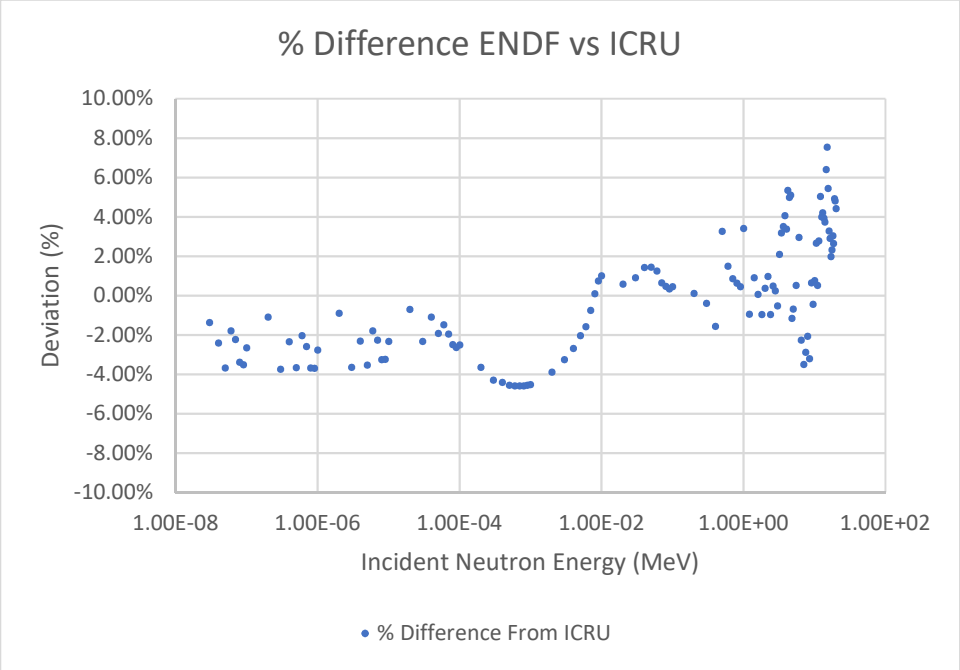

Figure 17: Percent difference from ICRU 63

In the 0.01 eV – 10 eV energy range (see Figure 18), the reaction that represents nearly the entire KERMA is the ^{14}N (n, p) ^{14}C reaction with some fraction of the total KERMA due to radiative capture with hydrogen and other elemental constituents. Generally, the methods utilized in this report are in strong agreement (2 - 4%) with ICRU 63 in this energy range.

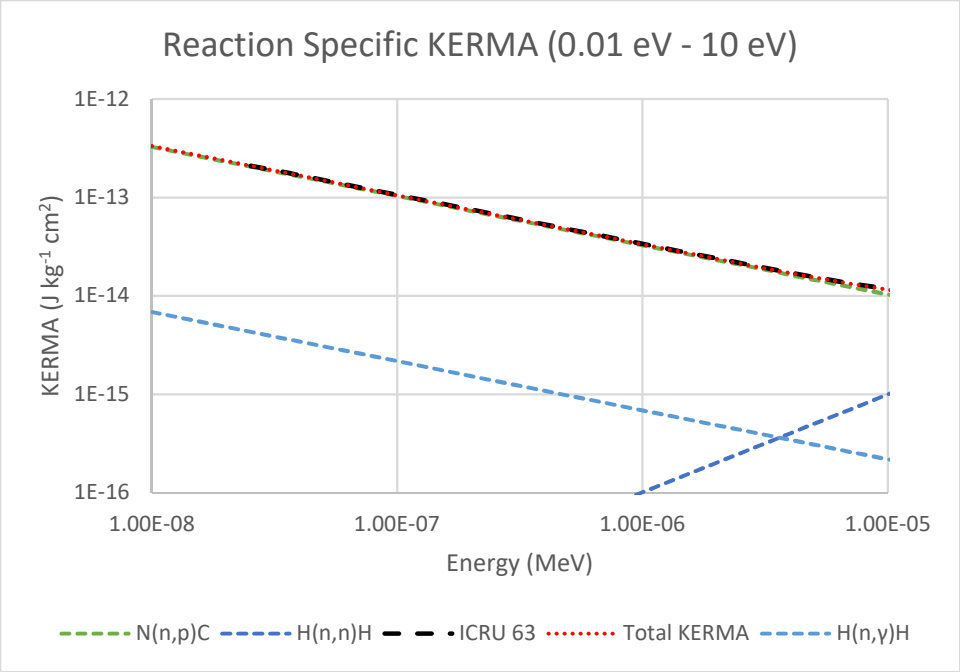

Figure 18: KERMA (0.01 eV - 10 eV)

As energy increases, the probability for these reactions decline. In the 10 eV – 10 keV energy range, i.e., the region where a noticeable dip is observed in the percent difference chart (Figure 17), the probability for elastic scatter dramatically increases such that the dominant reaction mechanism is elastic scatter with hydrogen. Resultant data is still in good agreement with ICRU 63 (Figure 19), however, the transition between these two reactions is a well-documented physical phenomenon such that any variation between methods will be represented systematically in the percent difference plot.

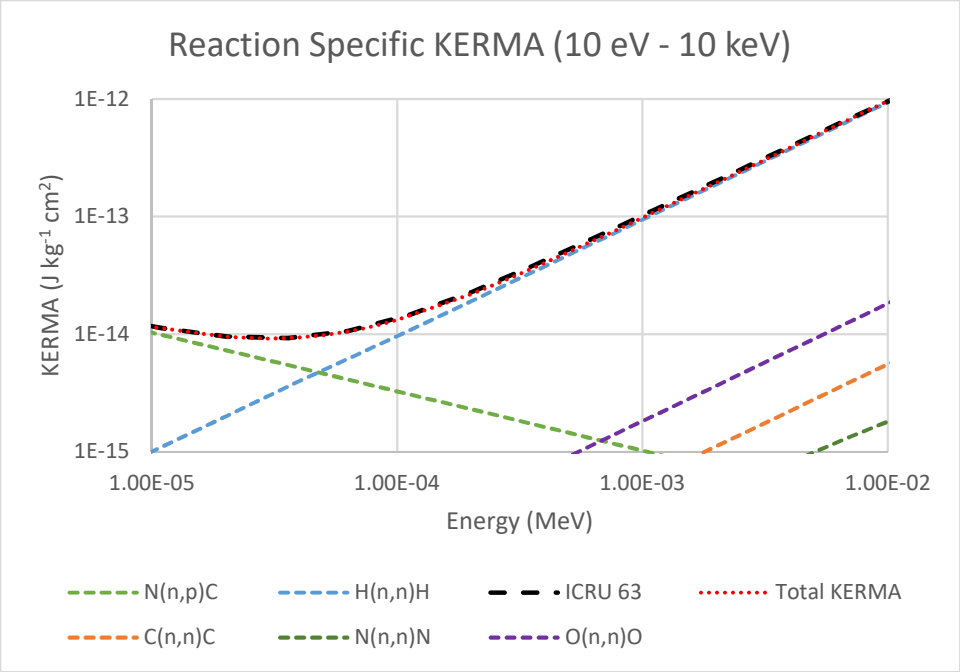

Figure 19: KERMA (10 eV - 10 keV)

Above 100 keV threshold inelastic scatter and transfer reactions constitute a significant portion of total KERMA. Variation in this region (see Figure 20) is primarily due to the different cross-sectional data utilized. Published in 2000, ICRU 63 bases their KERMA values off the ENDF/B-VI.0 evaluated cross sectional data. In this report, ENDF/B-VIII.0 is primarily used which was published in 2018 as opposed to 1992. Figure 20 demonstrates the complexity of neutron KERMA in this energy range (International Commission on Radiation Units and Measurements, 2000):

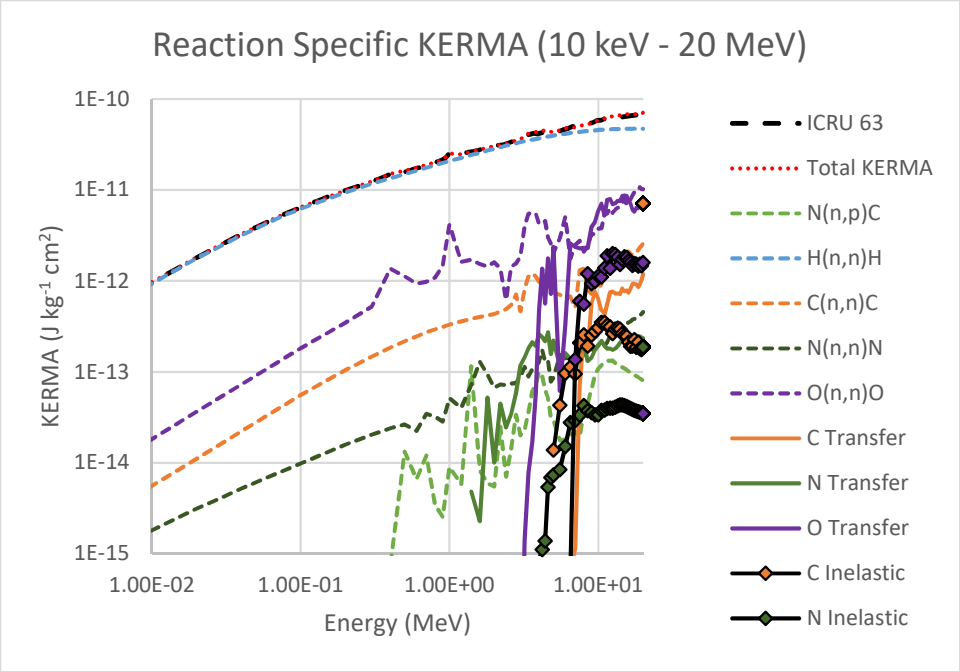

Figure 20: KERMA (10 keV - 20 MeV)

4.3 Radiative Photon Dose for Whole-Body Dosimetry

As discussed in Section 2.5, during whole-body exposure, photon generation is assumed to be uniformly distributed throughout the body. Pairing this method with the photon production cross sections pulled from the Evaluated Nuclear Data Files, the whole-body photon dose for a given reaction was determined. Summation over each evaluated photon-producing reaction yields the total whole-body photon dose during uniform exposure at a given incident neutron energy (see Figure 21).

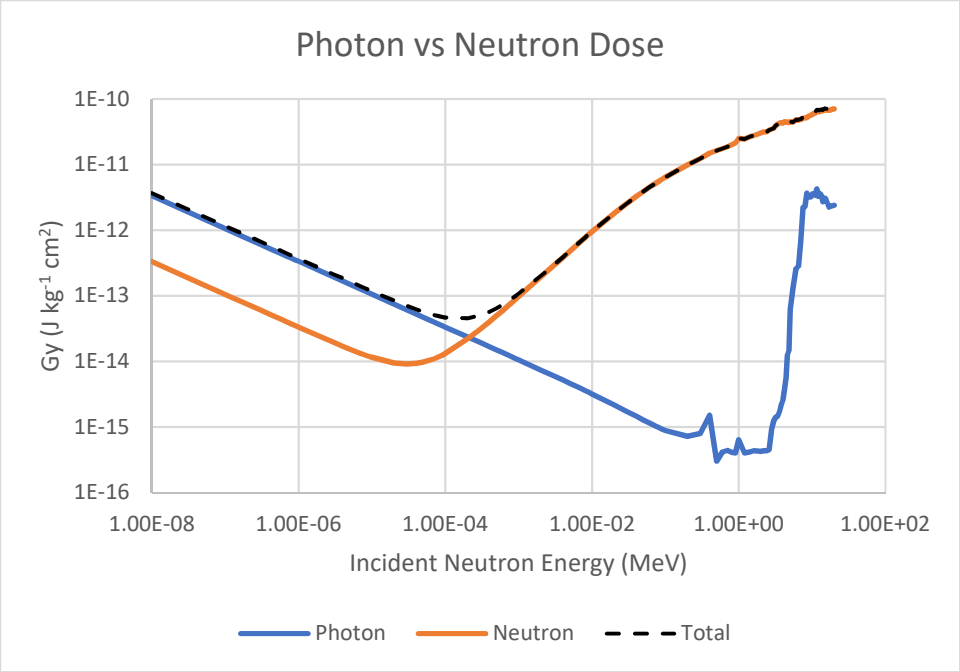

Figure 21: Whole-Body Photon vs Neutron Dose

This process is separate from shallow neutron dosimetry where the assumption of charged particle equilibrium is not valid for fast neutrons. In this case, local energy deposition in small tissue volumes is the primary concern for neutron dose. Photons generated in these small critical volumes have a very low probability of interaction and are assumed to leave the critical target in its entirety. However, for whole-body dosimetry where the tissue volume is many orders of magnitude larger than a 10-micron tissue segment, photon dose must be considered.

Below energies of 1 keV, the whole-body radiative photon dose is nearly an order of magnitude larger than the neutron dose. This is primarily due to the relatively large hydrogen capture cross section. The effect of generated photons drops off beyond this energy until approximately 1 MeV where threshold inelastic and transfer reactions start to occur. At this point the contribution to total dose from

primarily inelastic photons begins to climb until it is approximately an order of magnitude less than the contribution from neutrons.

5 Conclusion

Utilizing the methods and resources discussed in this report, a generalized shallow neutron dosimetry model is proposed herein:

$$H(d,E) = kW_r(E)f_{cpe}(d,E)\sum_j N_j \sum_i \epsilon_{ij}(E)\sigma_{ij}(E)\Phi(d,E) \qquad (21)$$

where $H(d,E)$ is the equivalent dose at a specific depth in tissue for a given neutron energy relative to a perpendicular fluence of neutrons to the tissue surface, k is the energy conversion factor $1.6022x10^{-13}\frac{J}{Mev}$, ϵ_{ij} is the energy transferred to charged particles as kinetic, and σ_{ij} is the microscopic cross section for nuclide j and interaction i. The number of atoms per unit mass of element j are represented by N_j and is defined by the ICRU 44 elemental composition of soft tissue. The radiation weighting factor for a given neutron at a specific energy is given by $W_r(E)$, while $\Phi(d,E)$ accounts for attenuation of the neutron fluence as governed by the Beer-Lambert law.

This research draws upon first-principles and existing cross-sectional data to develop a relatively straightforward depth-dependent neutron dosimetry model. More computationally rigorous tools (e.g., MCNP) can be utilized to determine neutron depth dose. However, as demonstrated herein, little variation between commonly accepted data published by the ICRU and recent studies utilizing MCNP exists. The variation that does exist is predominantly due to the utilization of different cross-sectional libraries.

Much of the focus of this research was to accurately develop a procedure to determine dose in shallow tissue regions where charged particle equilibrium is not established. A variety of neutron dosimetry procedures rely on the assumption that KERMA is equivalent to absorbed dose which is invalid in this critical target region for neutrons in the energy range of 1 – 20 MeV. Below 1 MeV charged particle equilibrium is established due to the relatively short range of recoil protons. This work demonstrates that charged particle equilibrium does not occur until the maximum range of an elastically scattered proton for a given incident neutron energy. As such, fractional charged particle equilibrium, f_{cpe}, describes the ratio between absorbed dose and KERMA at a given depth in tissue and corrects for the consideration of shallow depth. Because of this parameter, a simpler KERMA calculation can be achieved as opposed to a more complicated simulation.

Little has been published regarding neutron fractional charged particle equilibrium. Shih-Yew Chen and Arthur B. Chilton published two similar papers in 1979 and have been quoted throughout this report. Generally, their analysis of neutron depth-dose is in strong agreement with the data reported here. What variation exists between this work and theirs is primarily due to drastic differences in computational ability. Due to the processing power at the time, they were forced to limit their analysis to tissue segments of 1 mm whereas this report utilizes segment thicknesses of 5 – 10 microns.

There are several areas where future research should be directed. First, the constant reevaluation of cross-sectional information throughout the physics community will necessitate updating nuclear reaction data. This model relies upon

the most up-to-date cross-sectional data from the Evaluated Nuclear Data File for any given nuclear reaction. The difference between sets of cross-sectional information is frequently cited throughout this report as the underlying cause of discrepancy between sets of KERMA values. This is imperative for threshold reactions that occur within the 1 – 20 MeV energy range.

Likewise, future consideration for nuclear reactions included in the calculation of KERMA is necessary when updating cross-sectional information. For many threshold reactions, a plethora of excited states, each with their own associated cross section, are possible. In this report, those excited level cross sections for a specific nuclear reaction that are on a similar order of magnitude to the most probable excited level were analyzed. This excludes those reactions that are significantly less likely to occur. If analysis of a specific nuclear reaction is necessary, then evaluation of those cross sections should be included.

This also affects the evaluation of whole-body dose since photon production is associated with many of these excited levels. While the focus of this research was on shallow neutron dosimetry, a method for whole body dosimetry has been proposed:

$$H(E) = D_{\gamma}(E)W_{R_{\gamma}} + H_n(E) \tag{22}$$

where $D_{\gamma}(E)$ is the absorbed dose from all photons produced from nuclear reactions associated with a specific neutron energy and $W_{R_{\gamma}}$ is the radiation weighting factor for photons (1). The equivalent dose due to neutrons, $H_n(E)$, is described by the general neutron dosimetry model wherein charged particle equilibrium is assumed

to be established. As such, photon production associated with a given neutron energy is directly described by the cross sections utilized within this report. This is also subject to reevaluation of those cross sections when the model is updated or when specific nuclear reaction channels are investigated in more detail.

Finally, future research may focus on the influence of neutron generated photons especially considering that the ICRP 23 absorbed fractions only apply to photons below 4 MeV. For any photons with energy above 4 MeV, their respective absorbed fraction is assumed to be equivalent to 4 MeV. This yields a slight over approximation for dose associated with higher energy photons.

6 Bibliography

(A) Chen, S.-Y., & Chilton, A. B. (1979). Depth-Dose Relationship near the Skin Resulting from Parallel Beams of Fast Neutrons. *Radiation Research, 77*(1), 21-33.

(B) Chen, S.-Y., & Chilton, A. B. (1979). Calculation of Fast Neutron Depth-Dose in the ICRU Standard Tissue Phantom and the Derivation of Neutron Fluence-to-Dose-Index Conversion Factors. *Radiation Research, 78*(3), 335-370.

Atomic Heritage Foundation. (2014). *Atomic Accidents: Manhatan Project History.* Retrieved from Atomic Heritage Foundation: https://www.atomicheritage.org/history/atomic-accidents

Attix, F. H. (1986). *Introduction to Radiological Physics and Radiation Dosimetry.* New York: Wiley.

Caswell, R. S., & Coyne, J. J. (1972). Interaction of Neutrons and Secondary Charged Particles with Tissue: Secondary Charged Particle Spectra. *Radiation Research, 52*(3), 448-470.

Caswell, R. S., Coyne, J. J., & Randolph, M. L. (1980). Kerma Factors for Neutron Energies below 30 MeV. *Radiation Research, 83*(2), 217-254.

Cember, H., & Johnson, T. E. (2009). *Introduction to Health Physics.* The McGraw-Hill Companies, Inc.

Droual, R. (2020). *Chapter 4 - Integumentary System.* Modesto Junior College.

Hall, E. J., & Amato, J. G. (2012). *Radiobiology for the Radiologist.* Philadelphia, PA: Lippincott Williams & Wilkins.

International Atomic Energy Agency. (2020). *Evaluated Nuclear Data File*. Retrieved from IAEA Nuclear Data Section: https://www-nds.iaea.org/exfor/endf.htm

International Commission on Radiation Units and Measurements. (2000). ICRU Report 63: Nuclear Data for Neutron and Proton Radiotherapy and for Radiation Protection. *Journal of the ICRU, 32*(2).

International Commission on Radiological Protection. (1974). *ICRP 23: Report of the Task Group on Reference Man.* Pergamon Press.

International Commission on Radiological Protection. (2007). The 2007 Recommendations of the International Commission on Radiological Protection. *Annals of the ICRP, 37*(2-4).

Liu, Z., & Chen, J. (2008). New Calculations of Neutron Kerma Coefficients and Dose Equivalent. *Journal of Radiological Protection, 28*, 185-193.

Los Alamos National Laboratory. (2017). *MCNP User's Manual Version 6.2.* Los Alamos National Security.

McConn Jr, R. J., Gesh, C. J., Pagh, R. T., Rucker, R. A., & Williams III, R. G. (2011). *Radiation Portal Monitor Project: Compendium of Material Composition for Radiation Transport Modelling.* Richland, Washington: Pacific Northwest National Laboratory.

National Cancer Institute. (2018). *Anatomy of the Skin*. Retrieved from SEER Training Modules: https://training.seer.cancer.gov/melanoma/anatomy/

National Institute of Standards and Technology. (2019). *PSTAR: Stopping Power and Range-Tables for Protons*. Retrieved from https://physics.nist.gov/PhysRefData/Star/Text/PSTAR.html

Nave, C. (2017). *Discovery of the Neutron*. Retrieved from HyperPhysics: http://hyperphysics.phy-astr.gsu.edu/hbase/Particles/neutrondis.html

Ritts, J. J. (1968). Calculation of Neutron Fluence-to-Kerma Factors for the Human Body. *Nuclear technology, 7*(1), 89-99.

Shultis, J. K., & Faw, E. R. (2000). *Radiation Shielding.* La Grange Park, IL: American Nuclear Society.

Shultis, J. K., & Faw, R. E. (2011). *An MCNP Primer.* Manhattan, KS: Kansas State University.

Systat Software. (2020). *TableCurve 2D: Automated Curve Fitting Analysis*. Retrieved from Systat Software: https://systatsoftware.com/products/tablecurve-2d/

United States Nuclear Regulatory Commission. (2018). 10 CFR 20 Subpart C - Occupational Dose Limits. Retrieved from https://www.nrc.gov/reading-rm/doc-collections/cfr/part020/part020-1201.html

Zieb, K., Hughes, H. G., James, M. R., & Xu, X. G. (2018). Review of heavy charged particle transport in MCNP6.2. *Nuclear Instruments and Methods in Physics Research Section A*(886), 77-87.

Appendix A: Constituent Cross Sections and KERMA

For each nuclear reaction analyzed within this report, there are two sets of plots here. The first plot is the cross-sectional data pulled from the Evaluated Nuclear Data File and is designated (A). The second plot (B) is the resulting KERMA calculation vs energy for each reaction analyzed in this report.

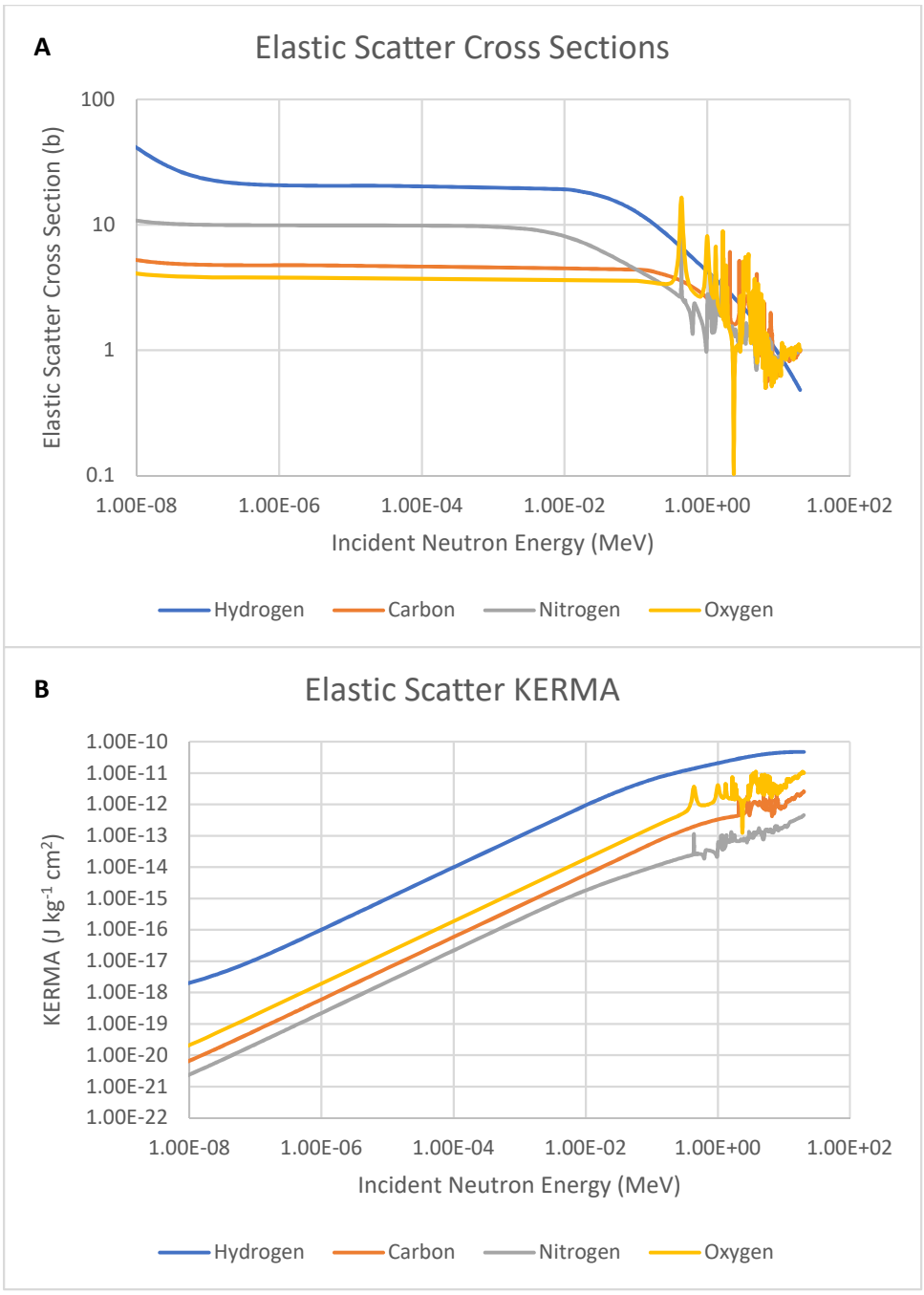

Figure A. 1: Elastic Scatter Cross Sections (a) and KERMA (b)

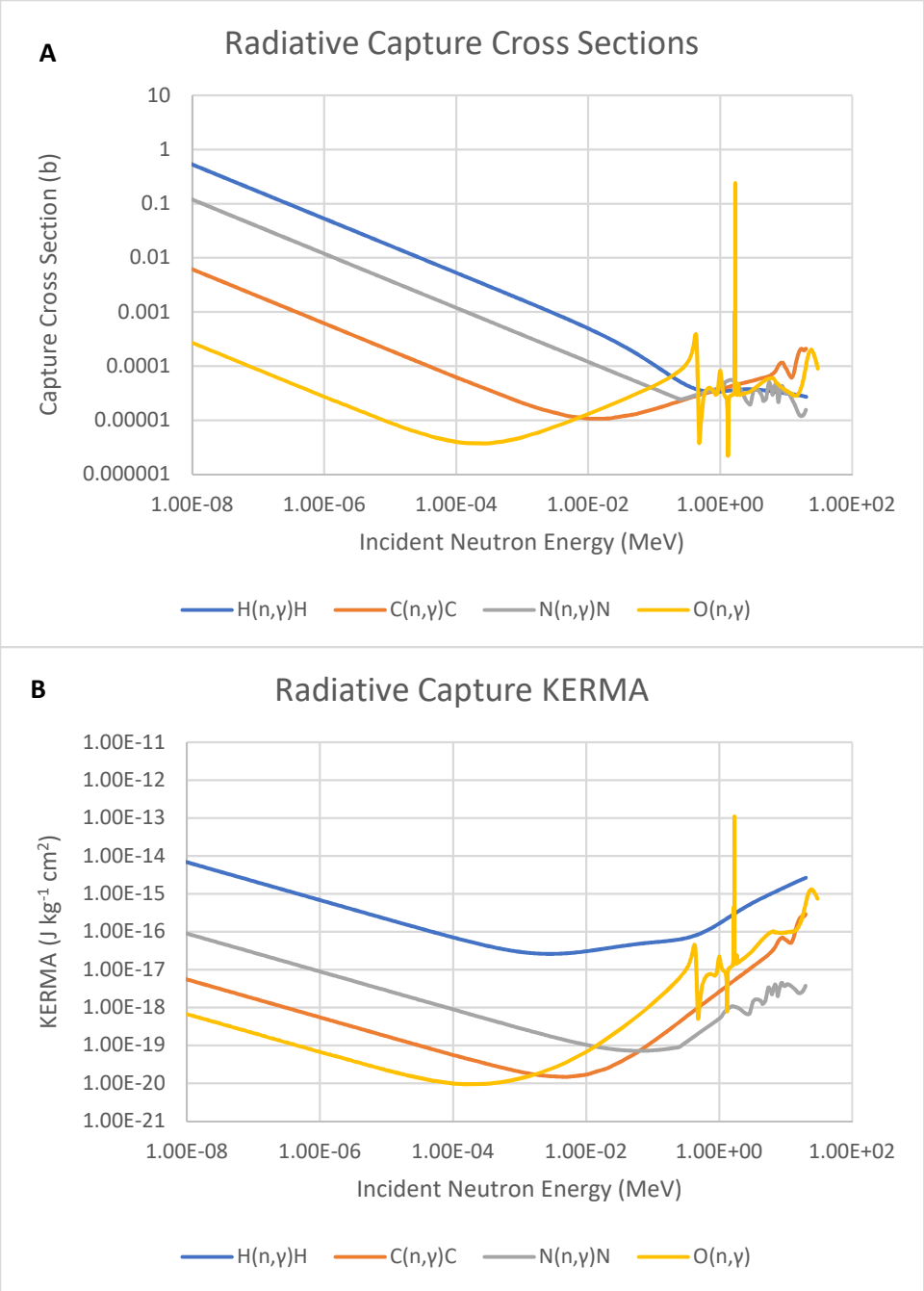

Figure A. 2: Radiative Capture Cross Sections (a) and KERMA (b)

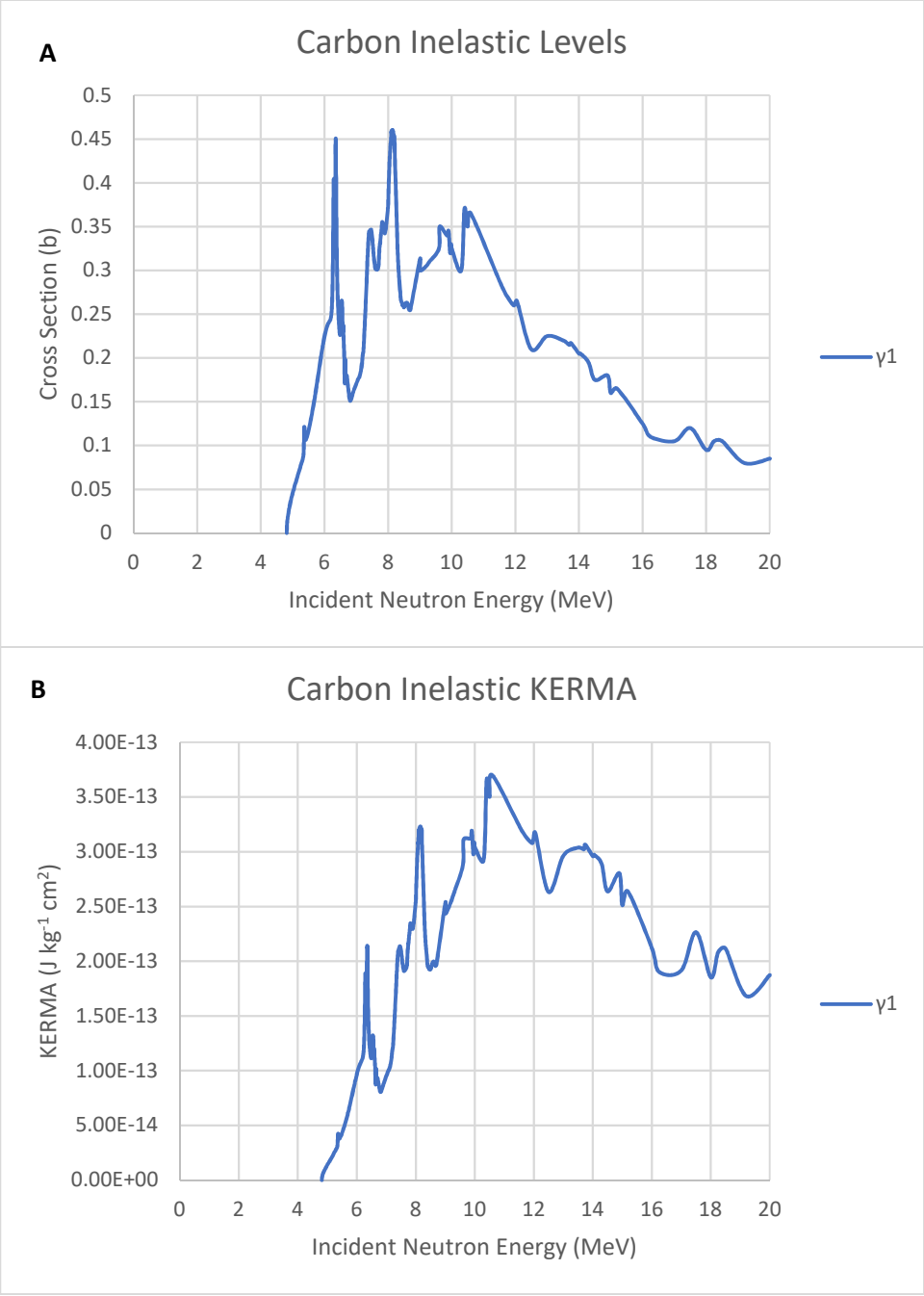

Figure A. 3: Carbon Inelastic Scatter Cross Section (a) and KERMA (b)

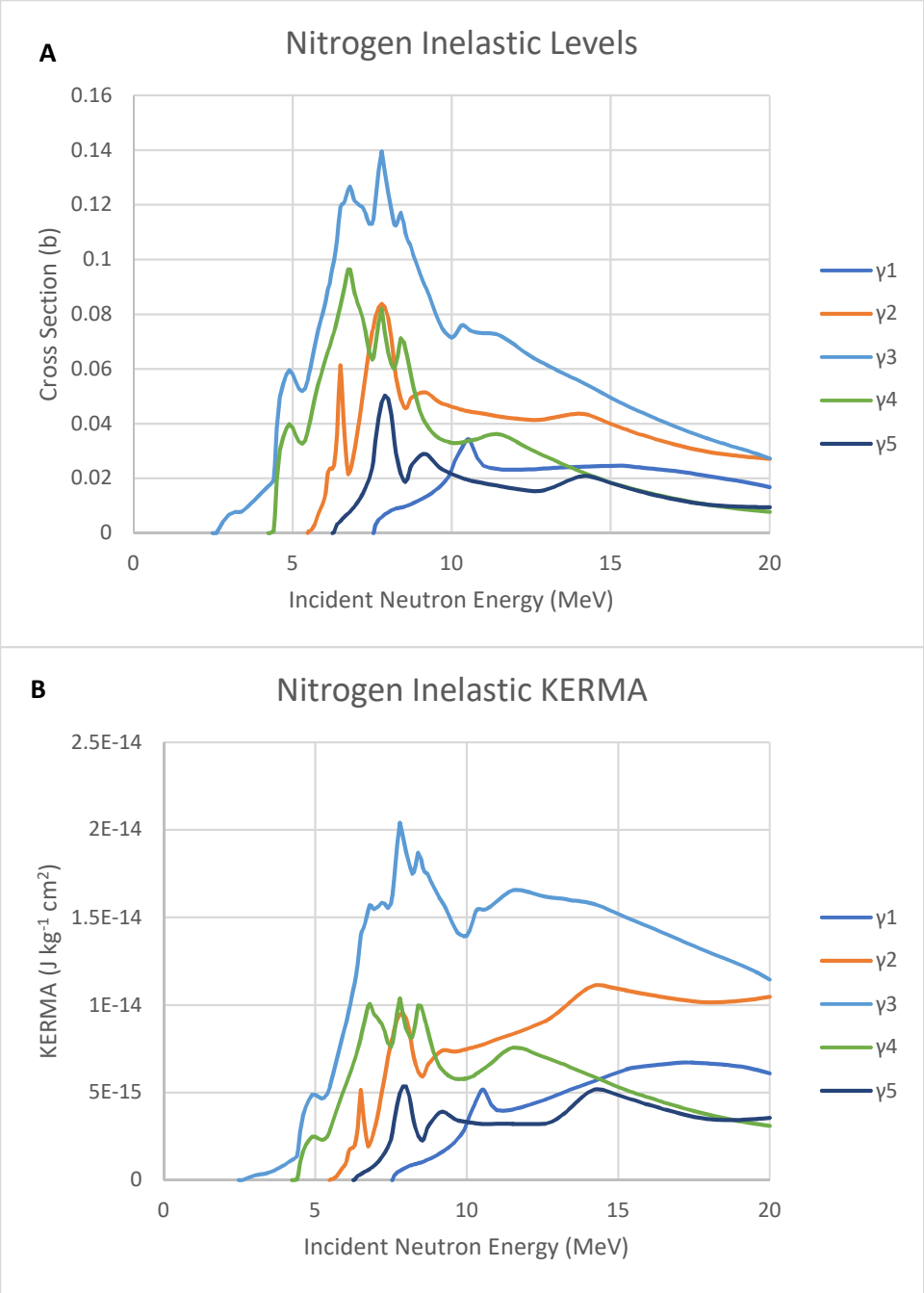

Figure A. 4: Nitrogen Inelastic Scatter Cross Sections (a) and KERMA (b)

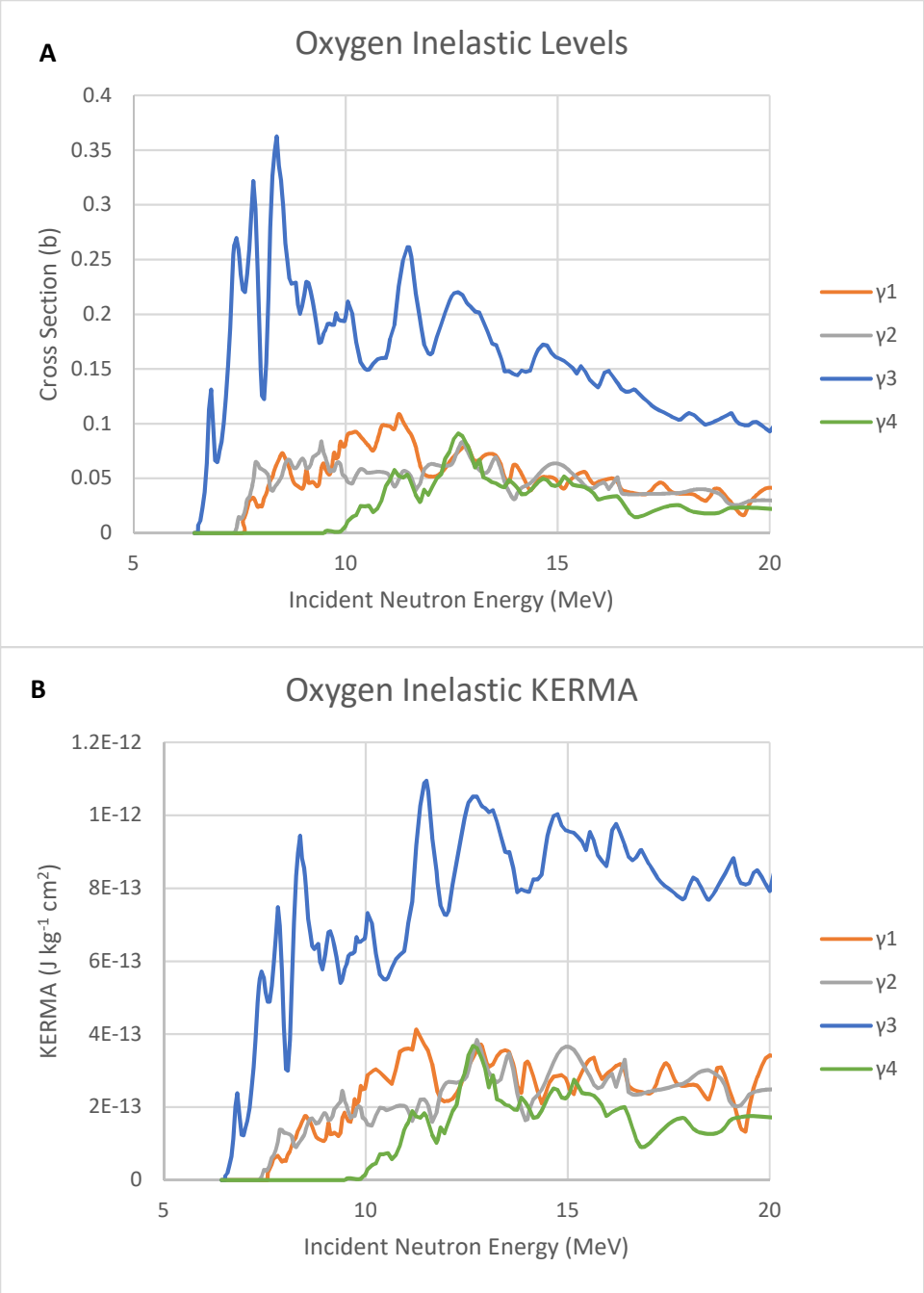

Figure A. 5: Oxygen Inelastic Scatter Cross Sections (a) and KERMA (b)

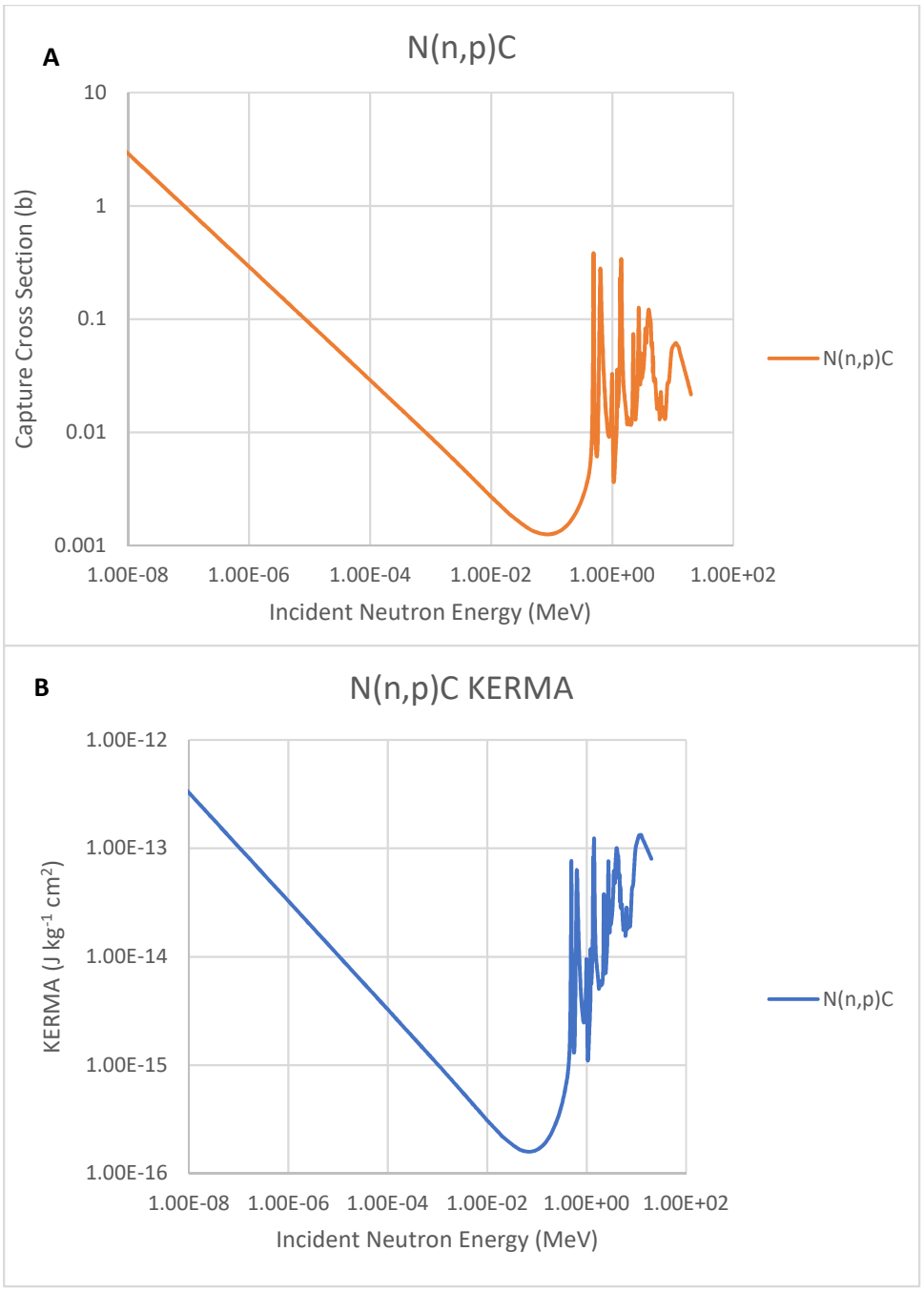

Figure A. 6: N (n, p) C Cross Section (a) and KERMA (b)

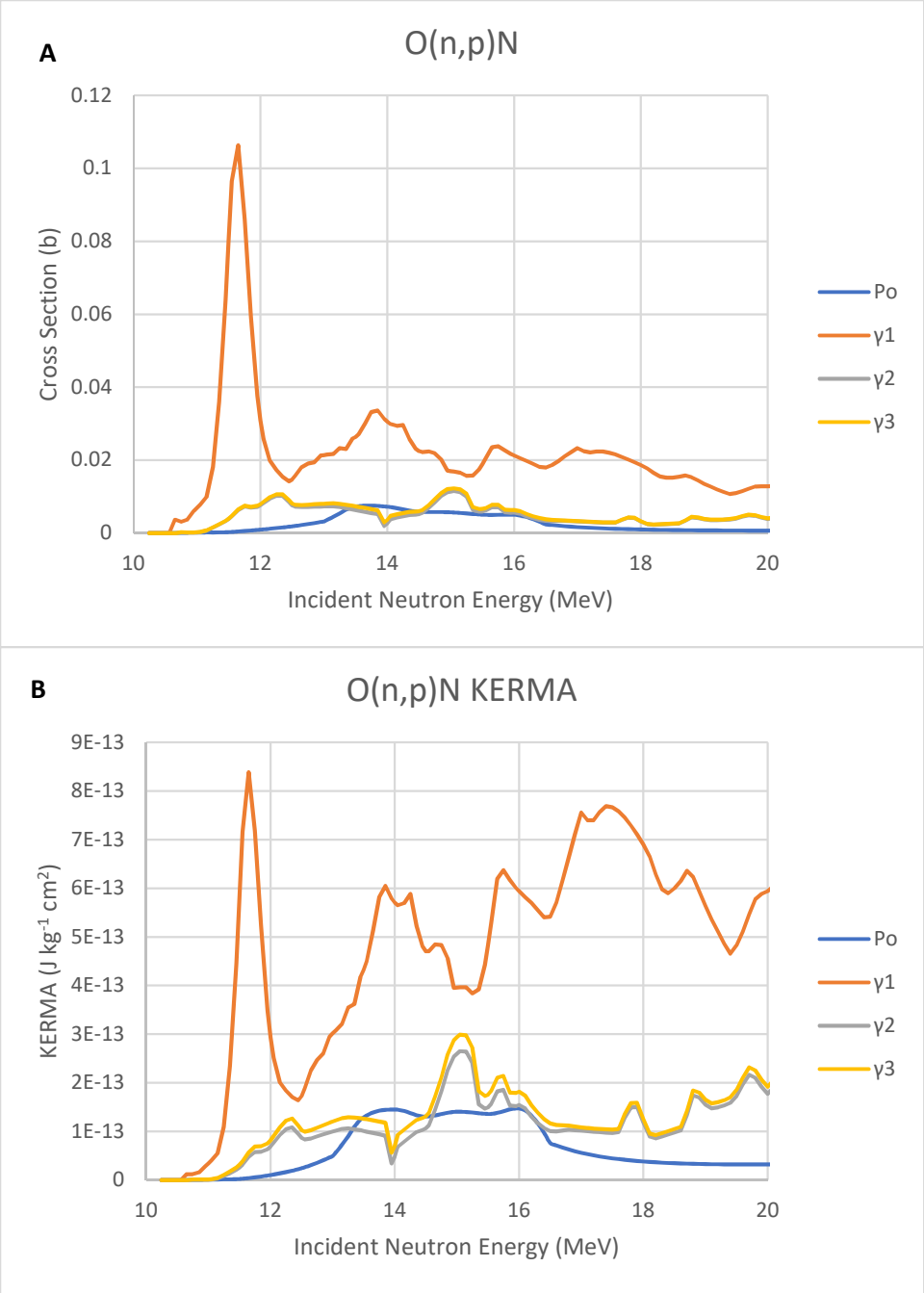

Figure A. 7: O (n, p) N Cross Sections (a) and KERMA (b)

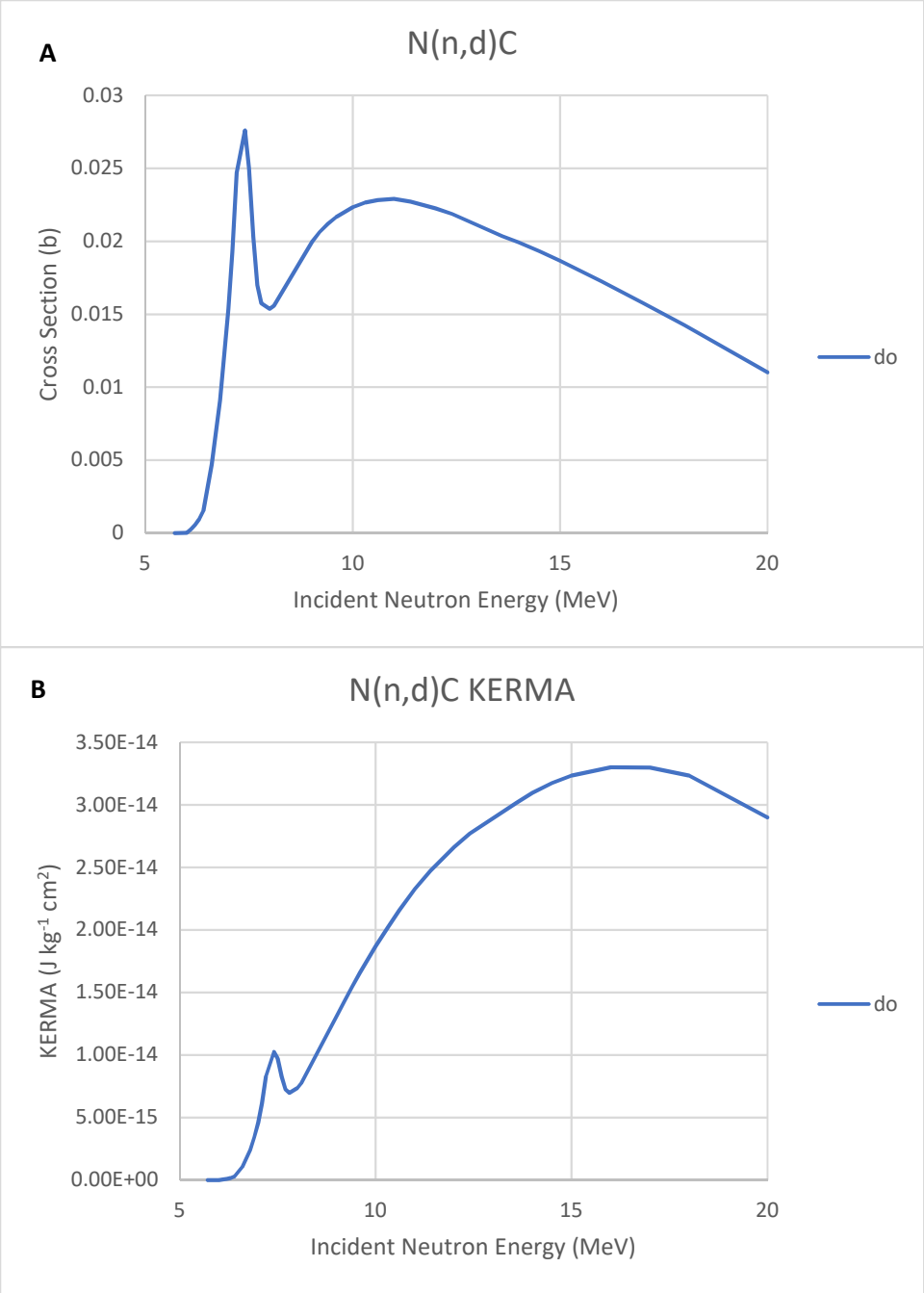

Figure A. 8: N (n, d) C Cross Sections (a) and KERMA (b)

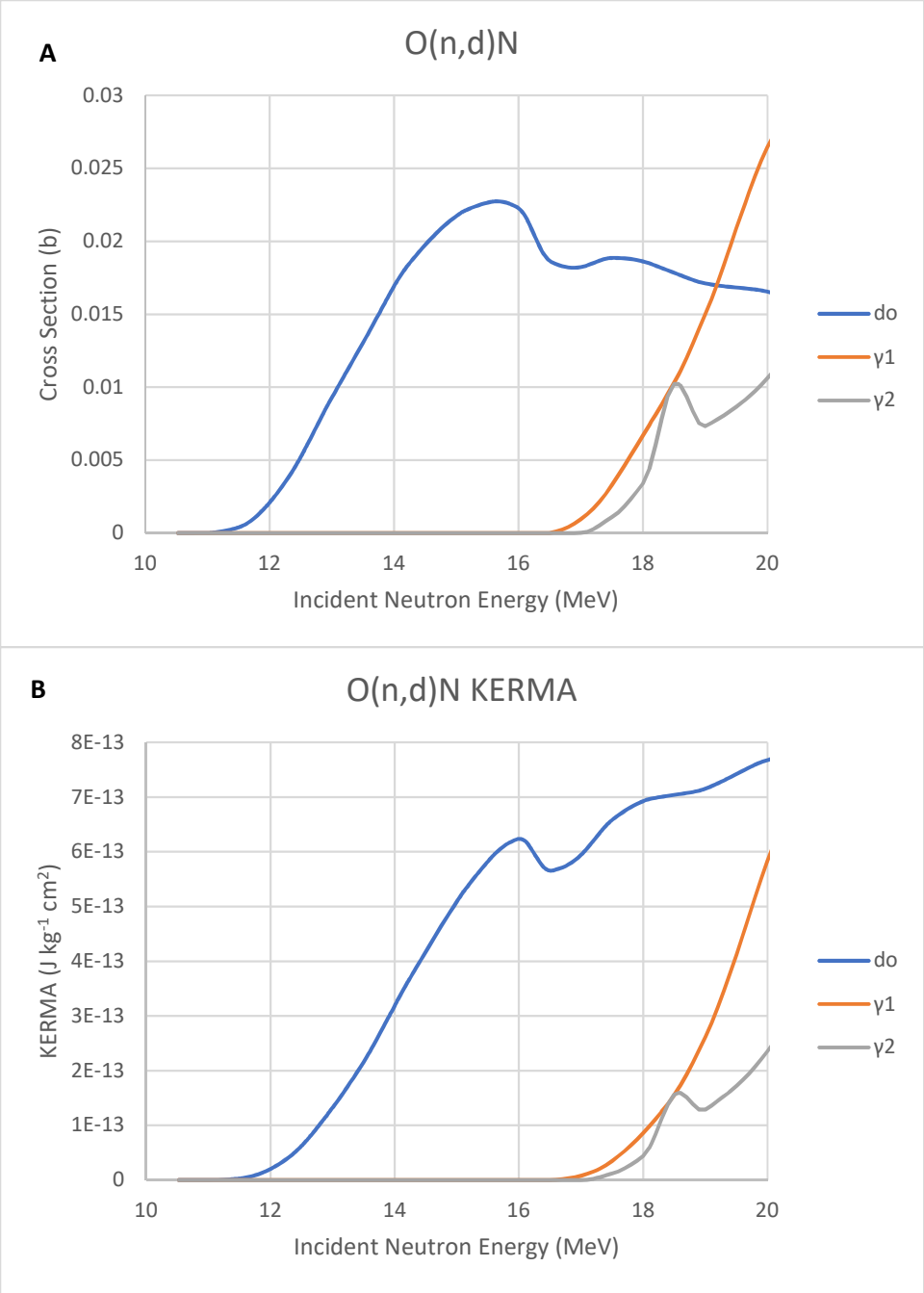

Figure A. 9: O (n, d) N Cross Sections (a) and KERMA (b)

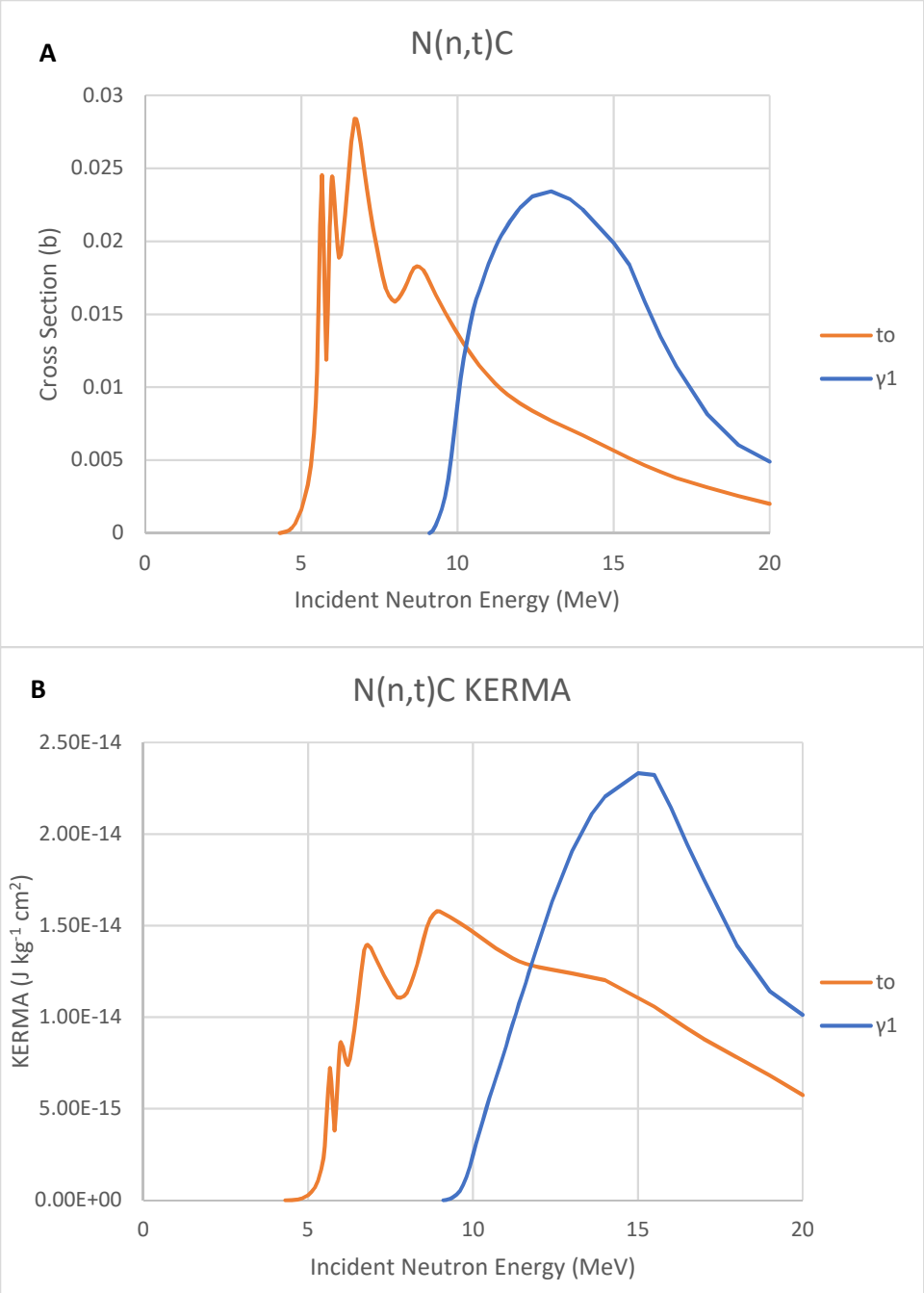

Figure A. 10: N (n, t) C Cross Sections (a) and KERMA (b)

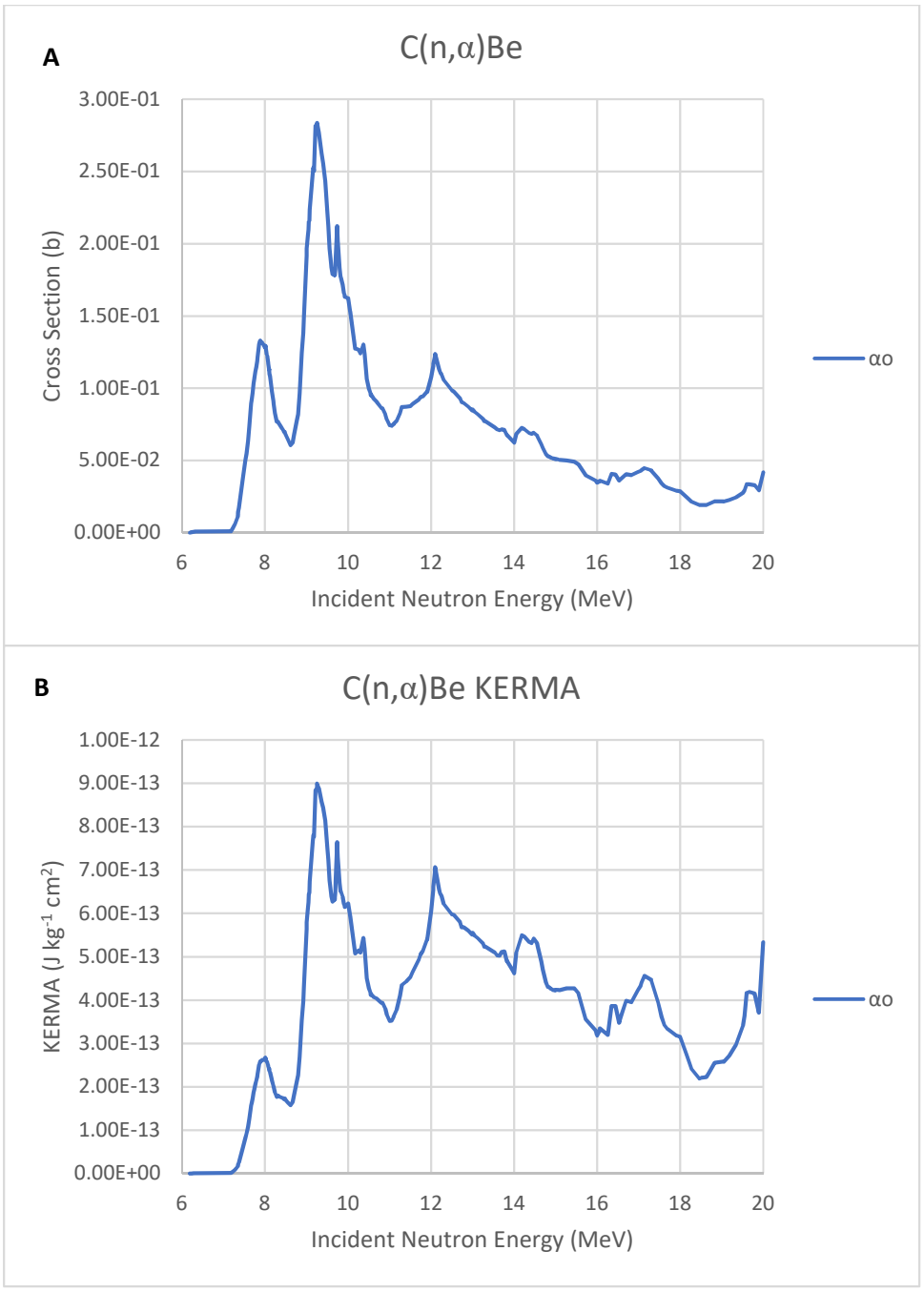

Figure A. 11: C (n, α) Be Cross Sections (a) and KERMA (b)

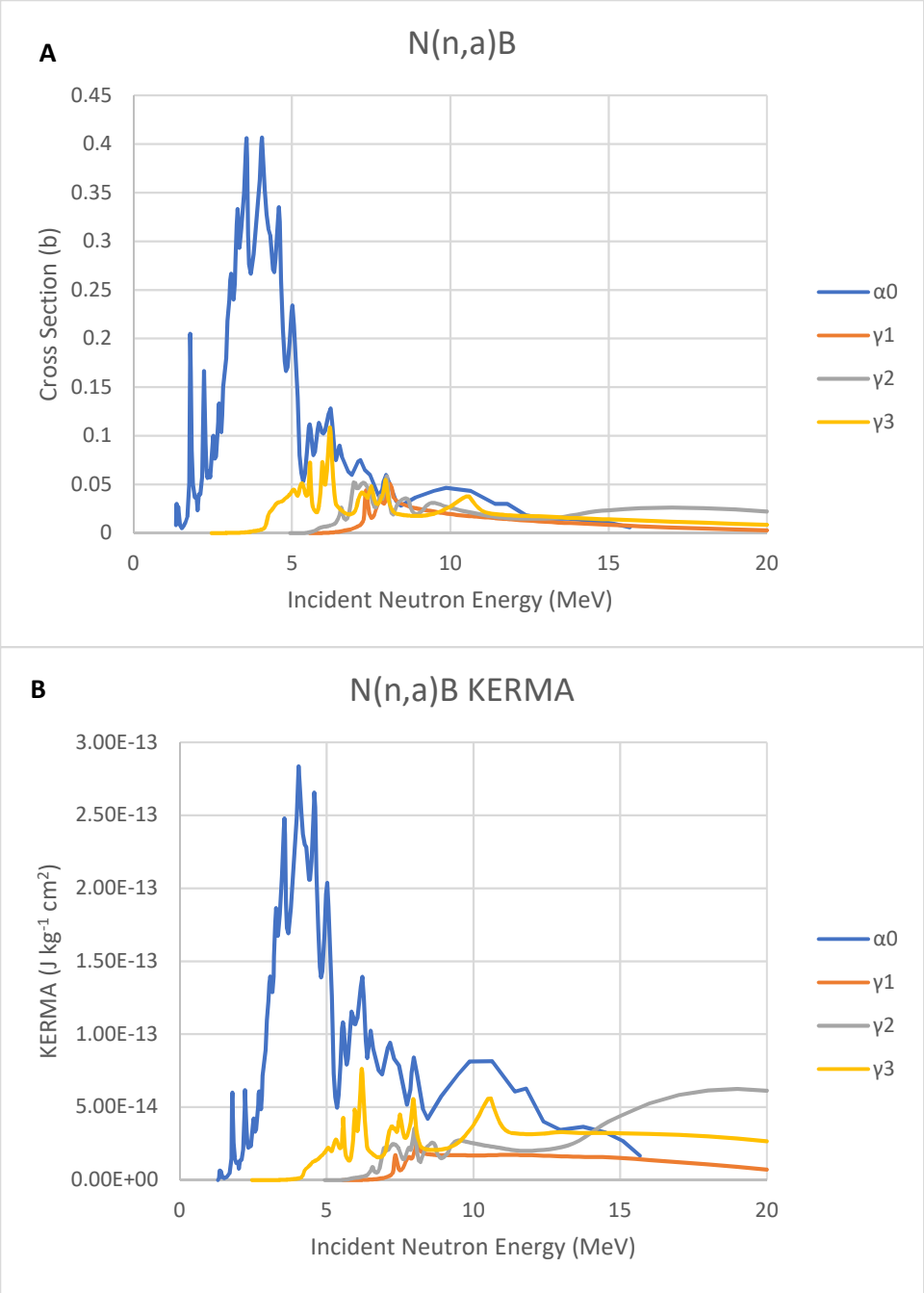

Figure A. 12: N (n, a) Be Cross Sections (a) and KERMA (b)

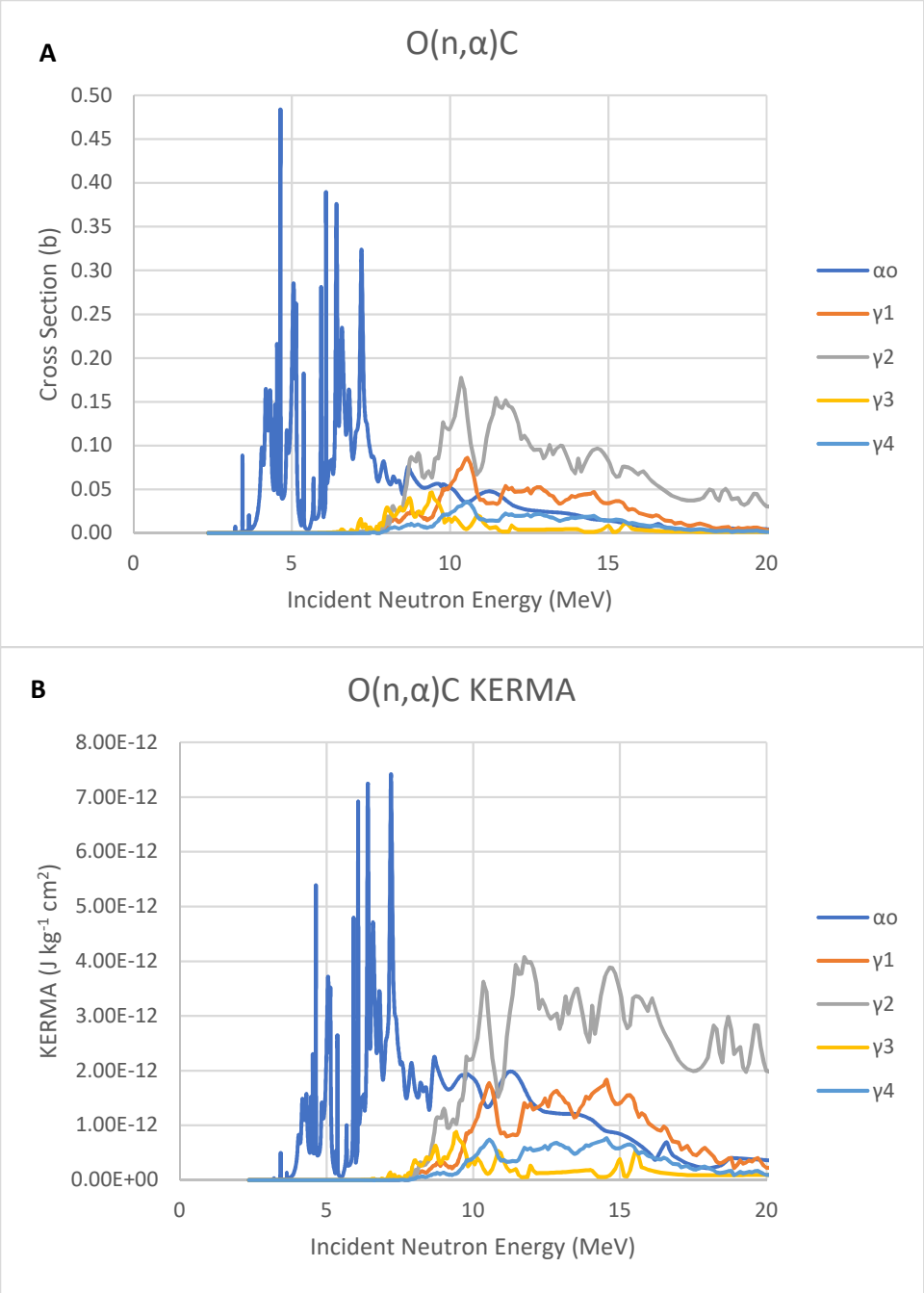

Figure A. 13: O (n, a) C Cross Sections (a) and KERMA (b)

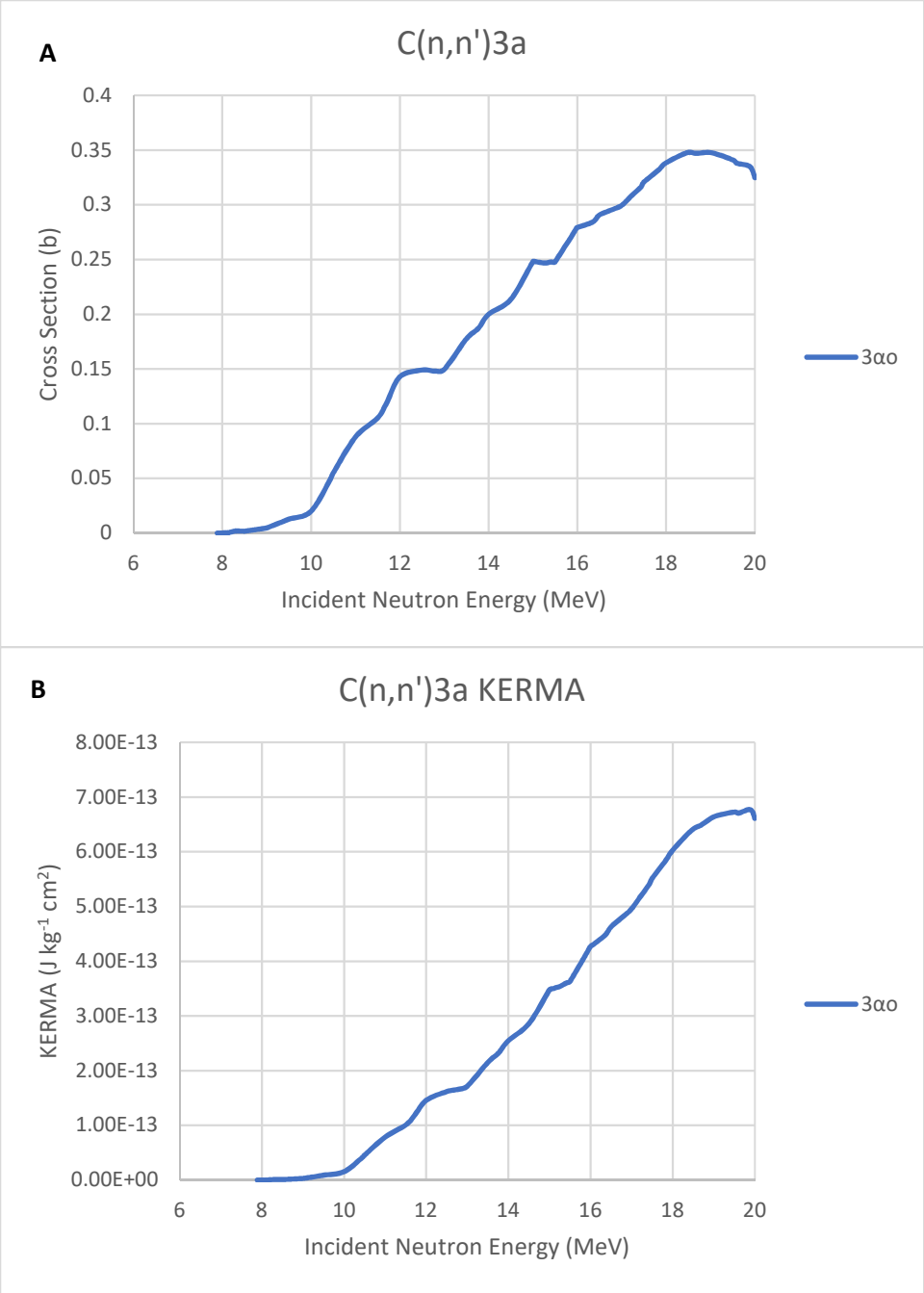

Figure A. 14: C (n, n') 3a Cross Sections (a) and KERMA (b)

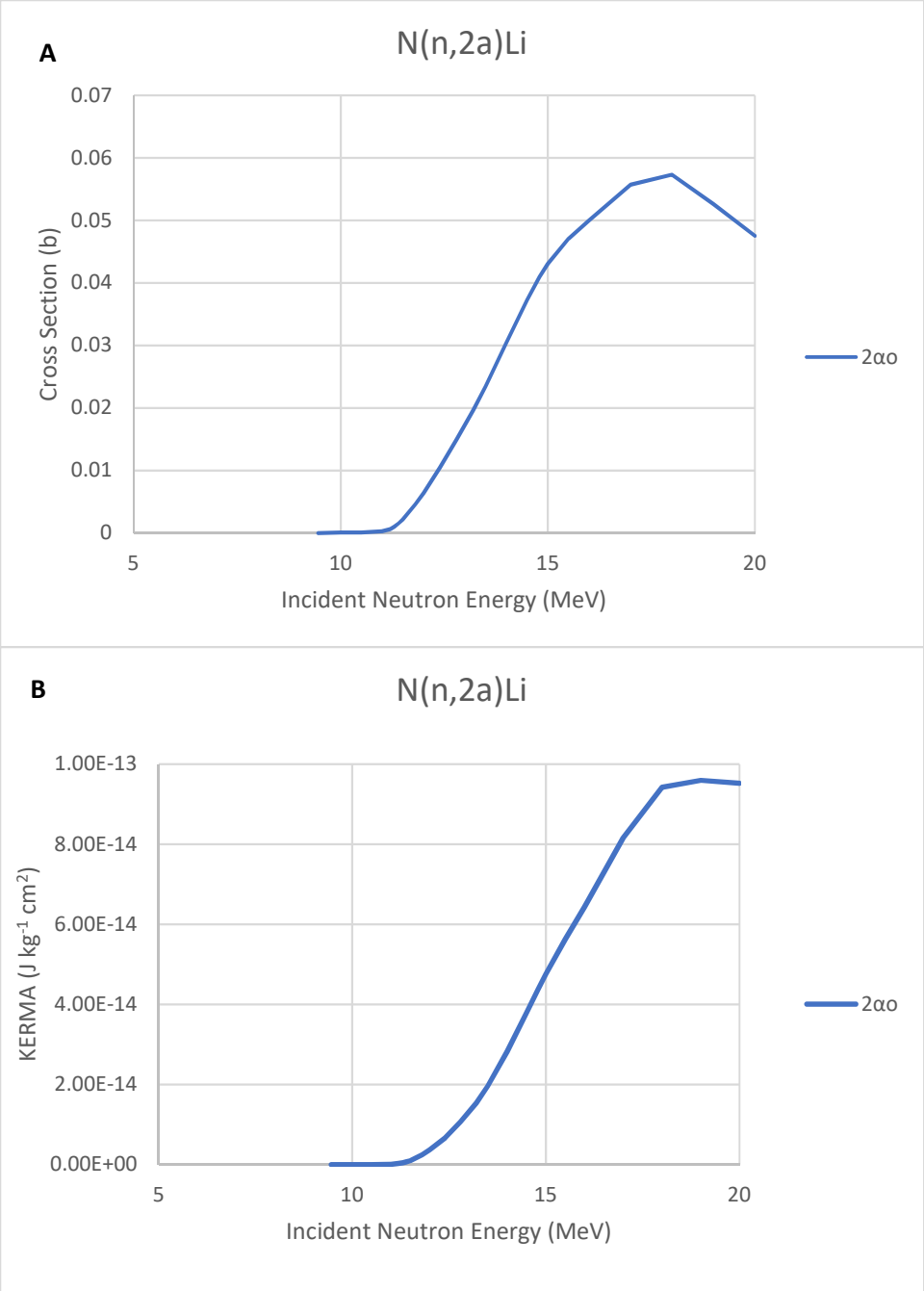

Figure A. 15:N (n, 2a) Li Cross Sections (a) and KERMA (b)

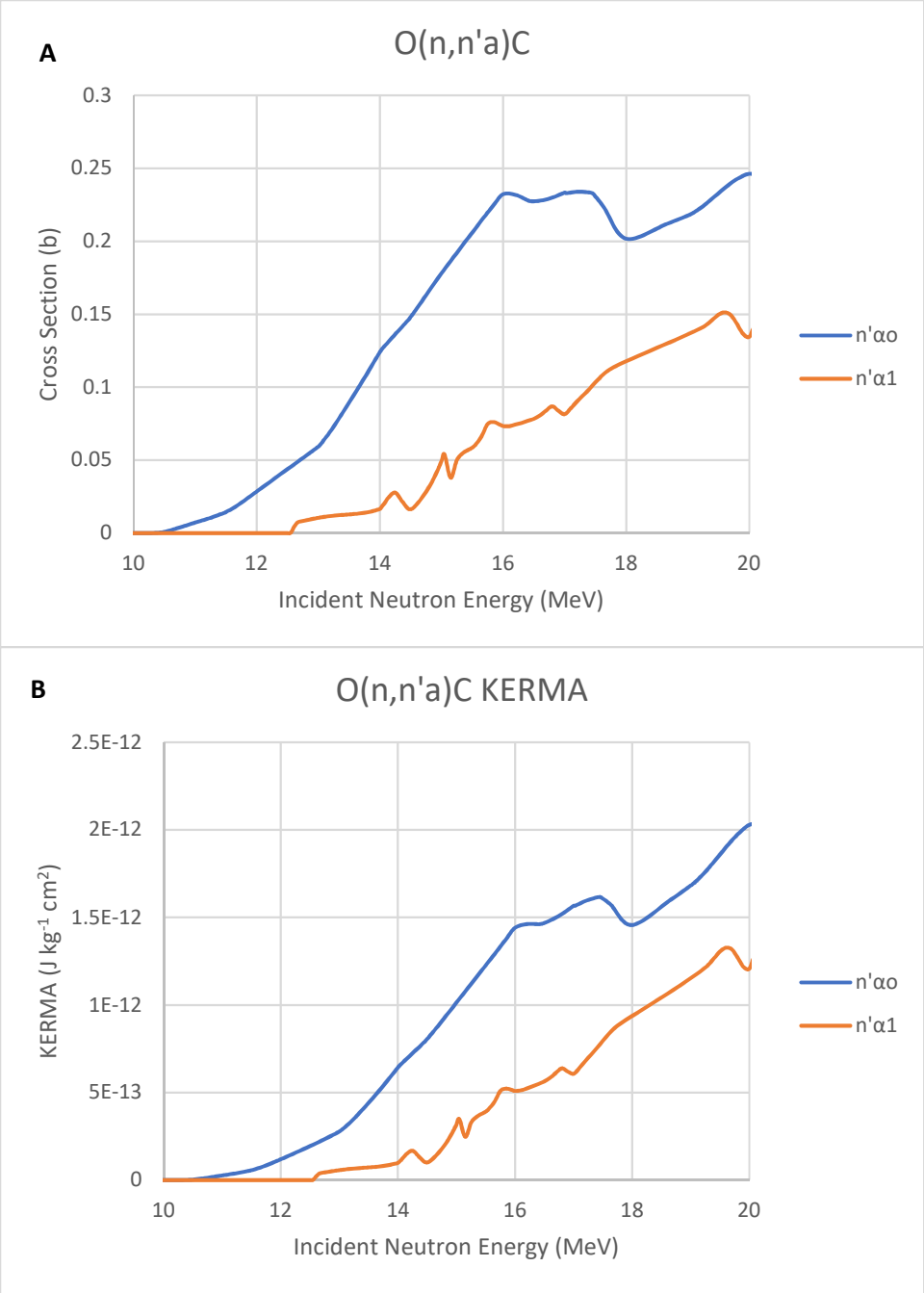

Figure A. 16: O (n, n'a) C Cross Sections (a) and KERMA (b)

Appendix B:Fractional Charged Particle Equilibrium Data

The subsequent plots represent two values. First, the resulting MCNP data for fractional charged particle equilibrium from all simulation conducted. Overlaid on each plot are the equations discussed in chapter 4 that were generated from the MCNP data in TableCurve2D. On several charts, as done in chapter 4, several comparisons are made to existing data produced by Shih-Yew Chen and Arthur B. Chilton in 1979.

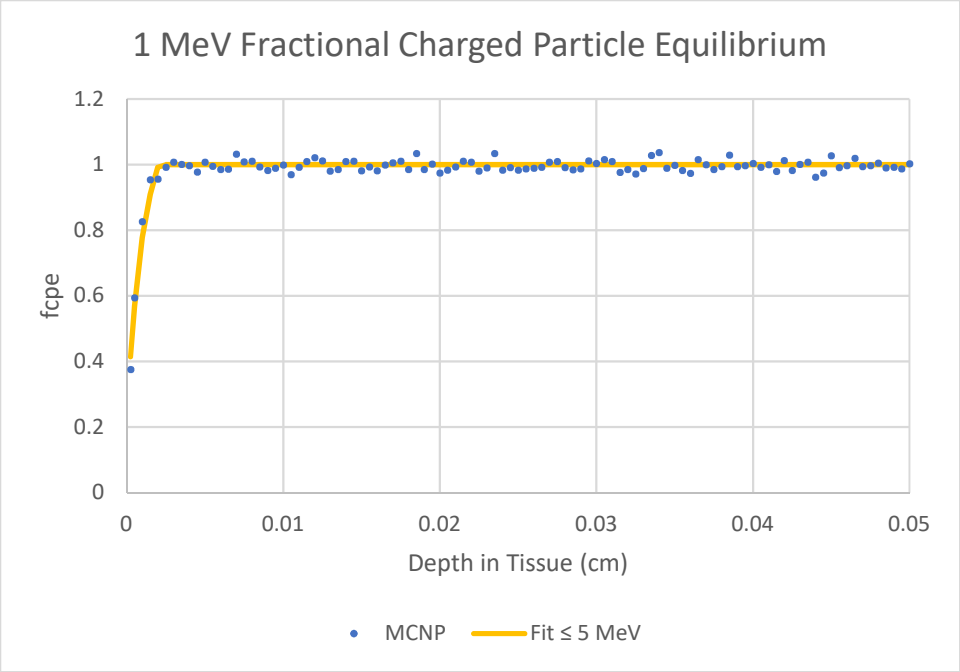

Figure A. 17: Fractional Charged Particle Equilibrium at 1 MeV

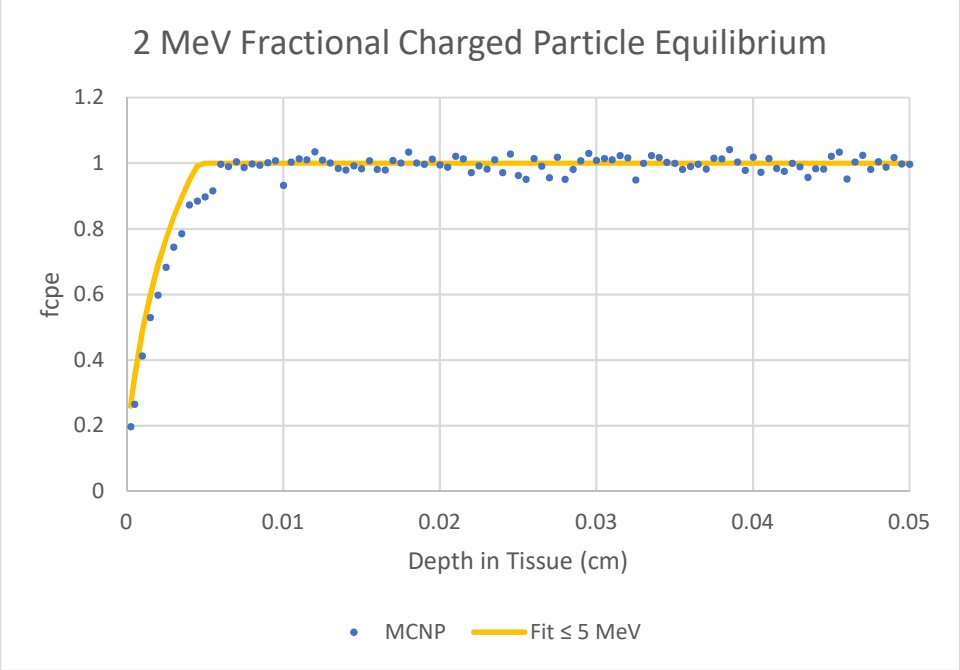

Figure A. 18: Fractional Charged Particle Equilibrium at 2 MeV

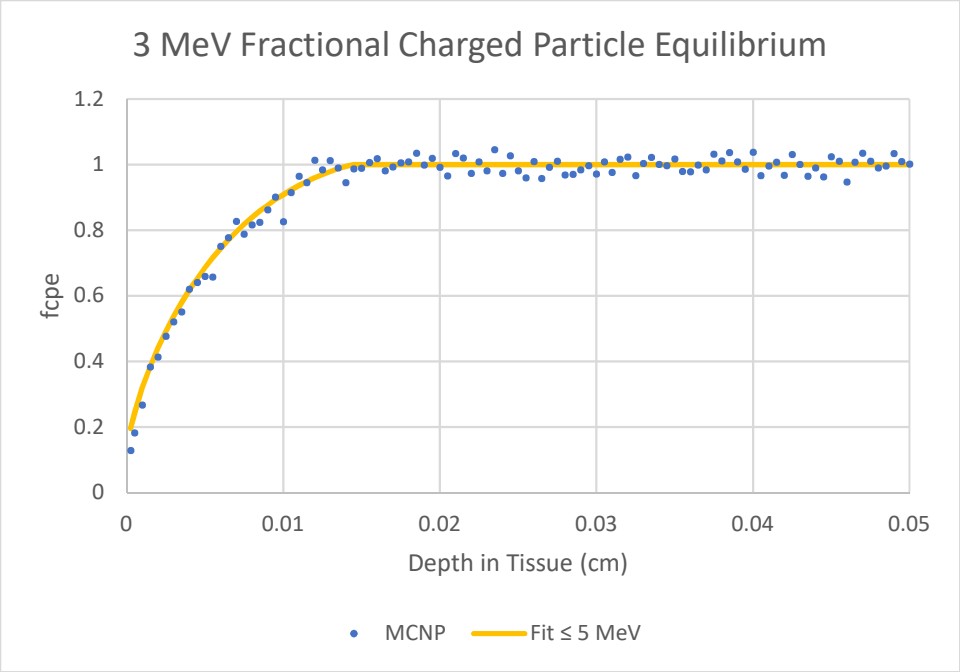

Figure A. 19: Fractional Charged Particle Equilibrium at 3 MeV

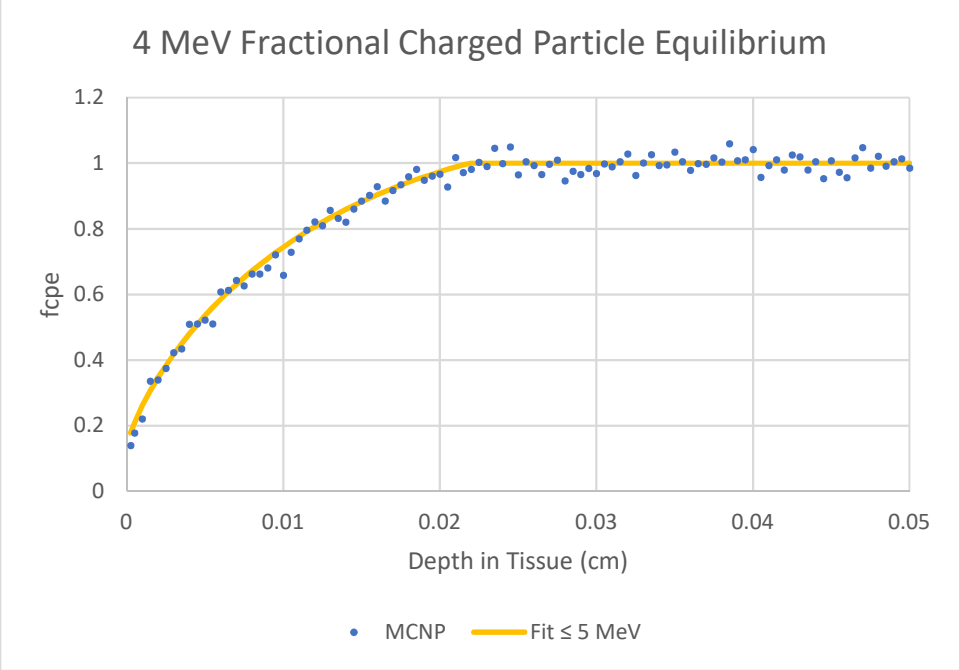

Figure A. 20: Fractional Charged Particle Equilibrium at 4 MeV

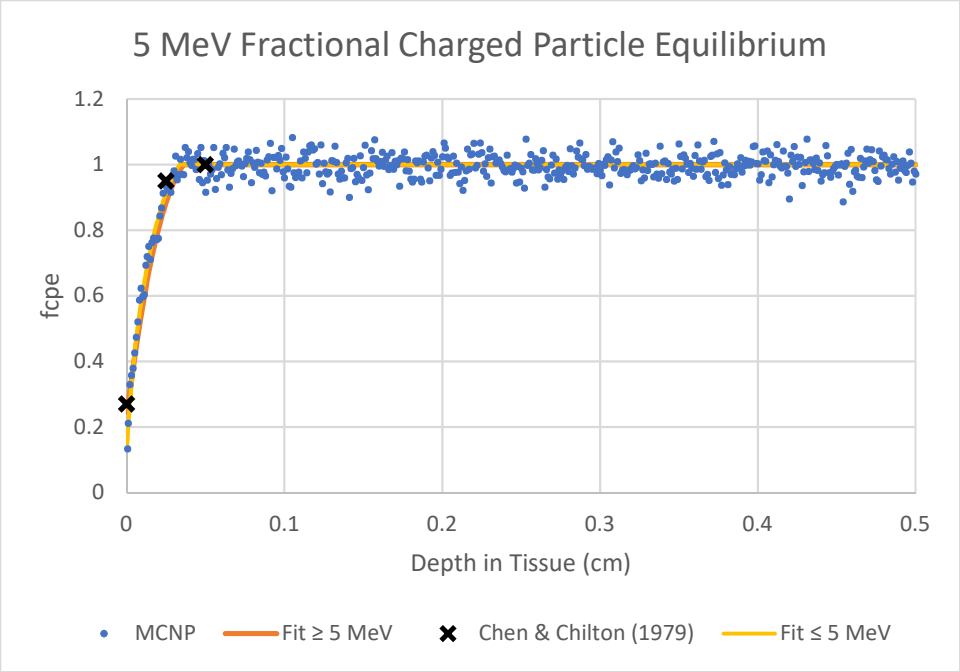

Figure A. 21: Fractional Charged Particle Equilibrium at 5 MeV

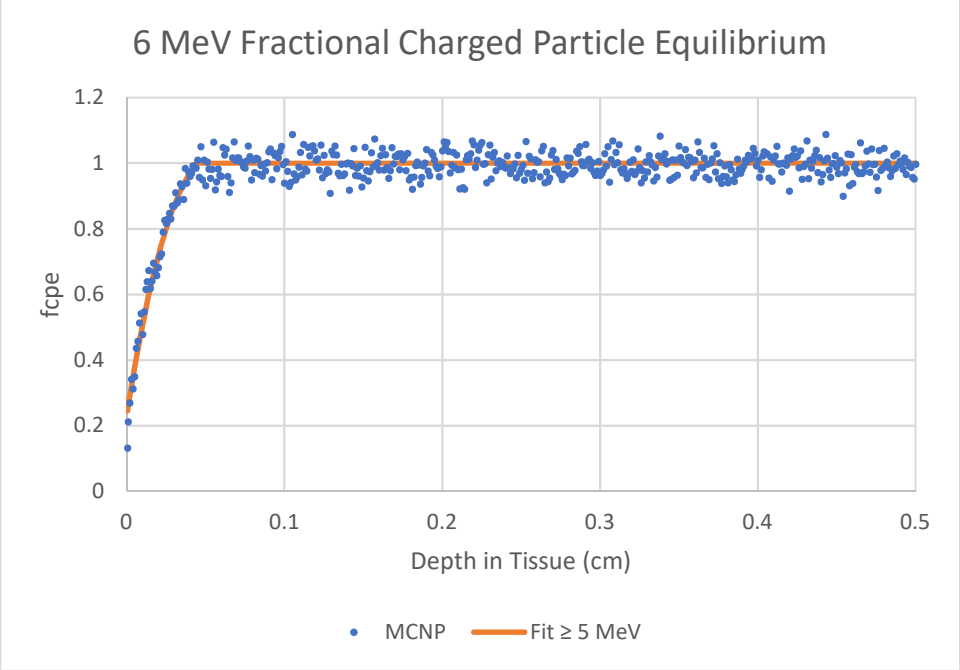

Figure A. 22: Fractional Charged Particle Equilibrium at 6 MeV

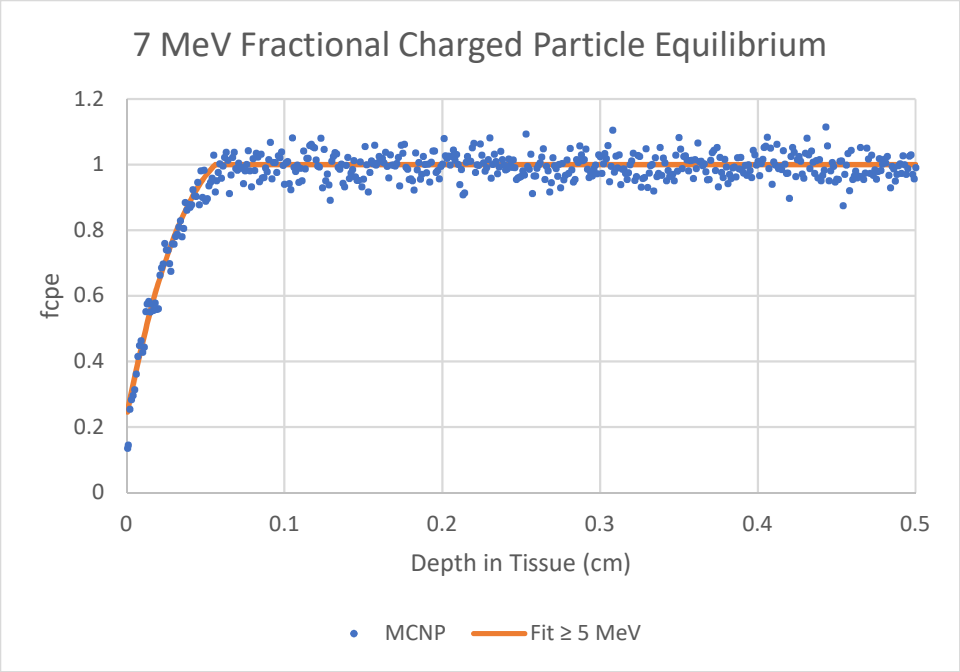

Figure A. 23: Fractional Charged Particle Equilibrium at 7 MeV

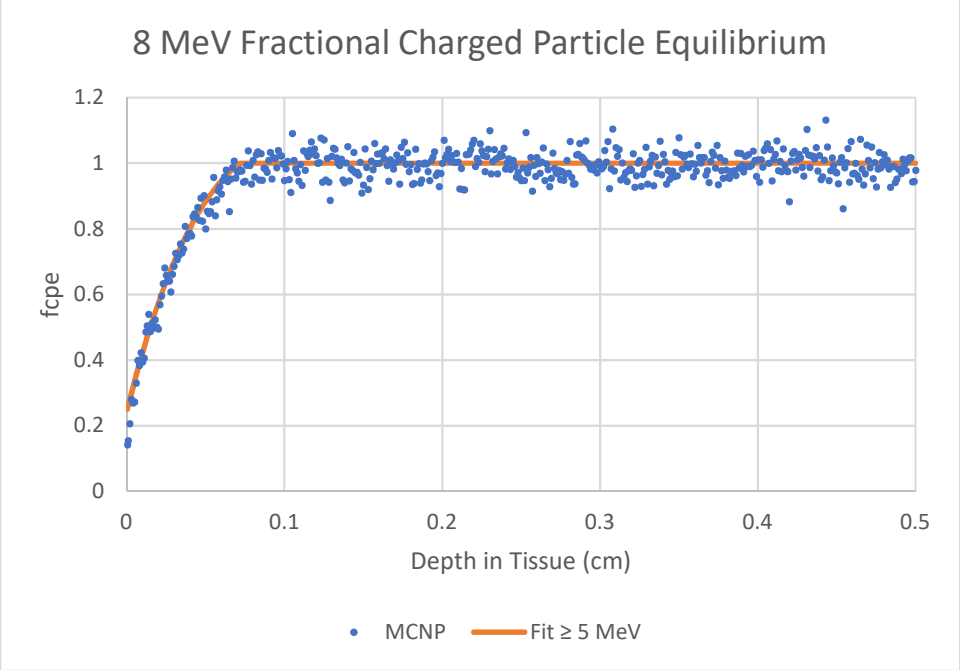

Figure A. 24: Fractional Charged Particle Equilibrium at 8 MeV

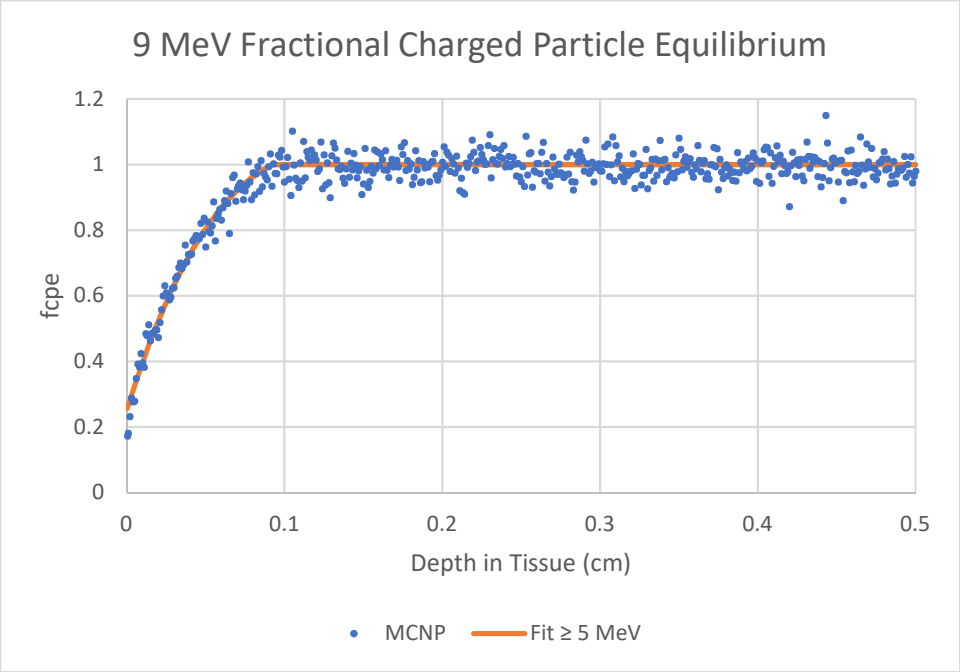

Figure A. 25: Fractional Charged Particle Equilibrium at 9 MeV

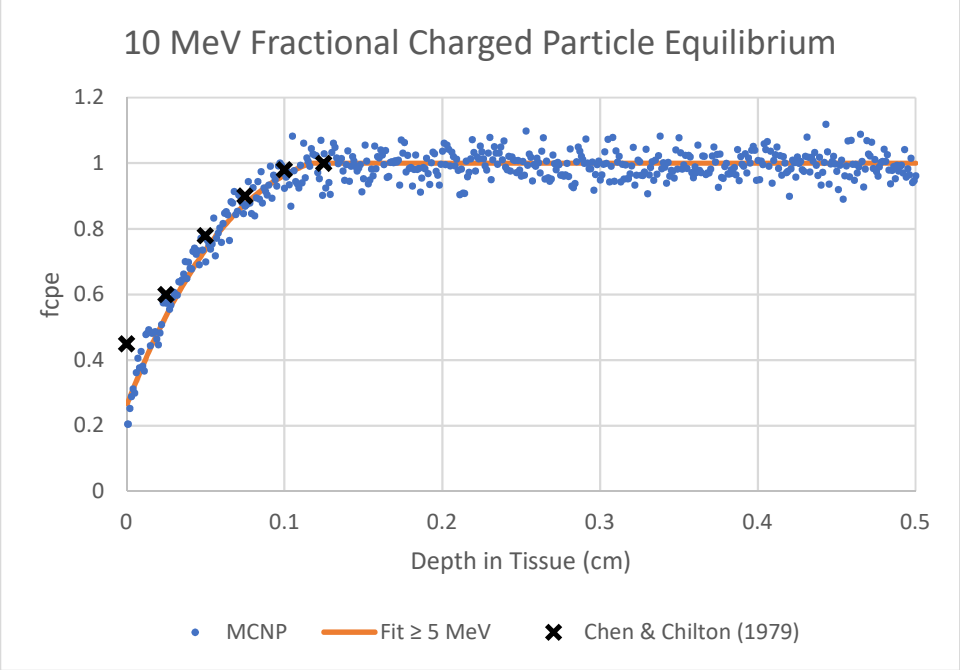

Figure A. 26: Fractional Charged Particle Equilibrium at 10 MeV

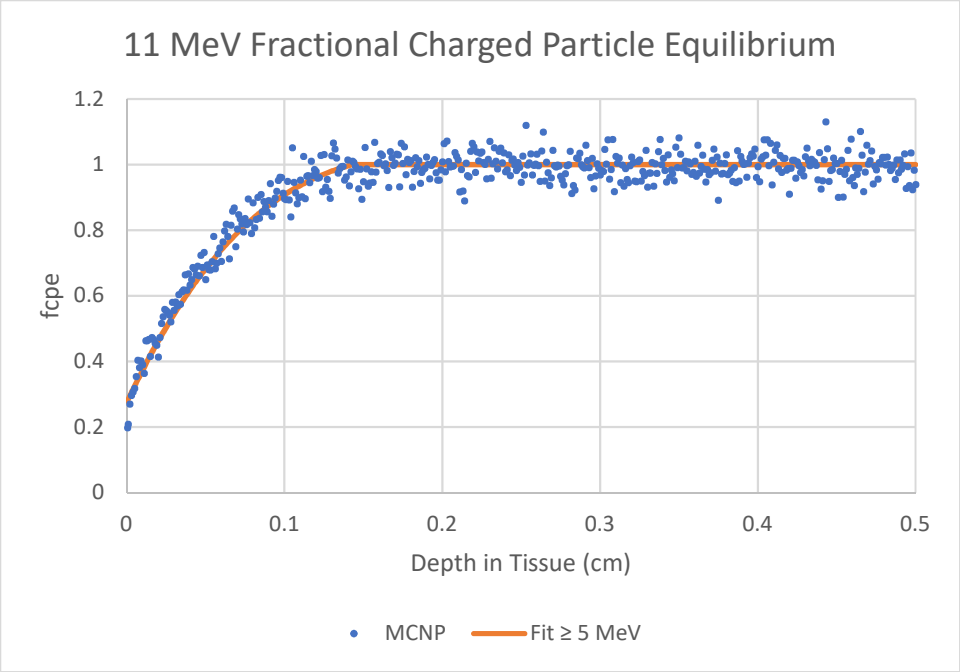

Figure A. 27: Fractional Charged Particle Equilibrium at 11 MeV

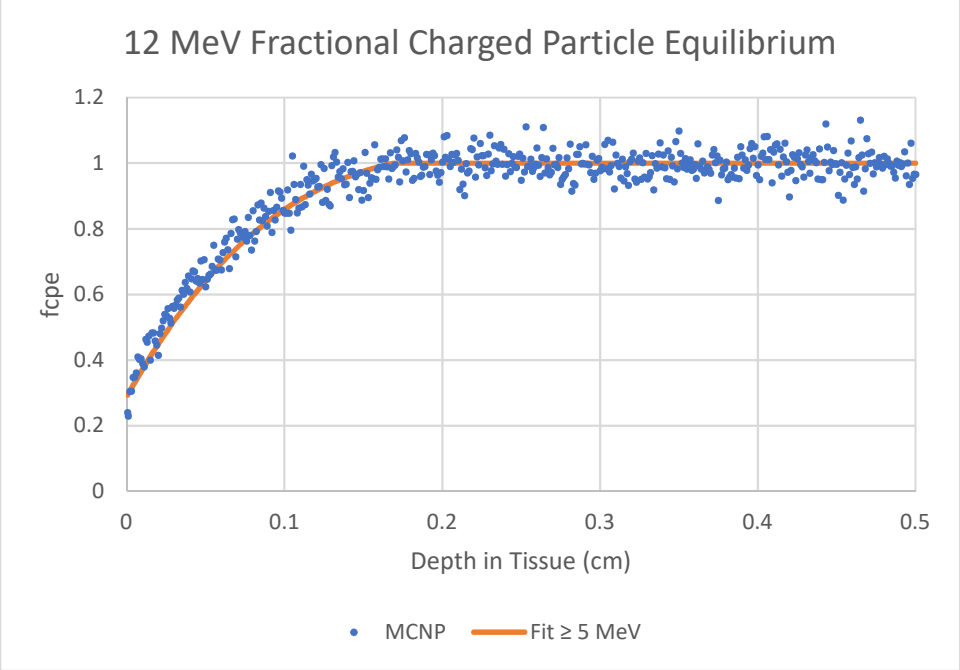

Figure A. 28: Fractional Charged Particle Equilibrium at 12 MeV

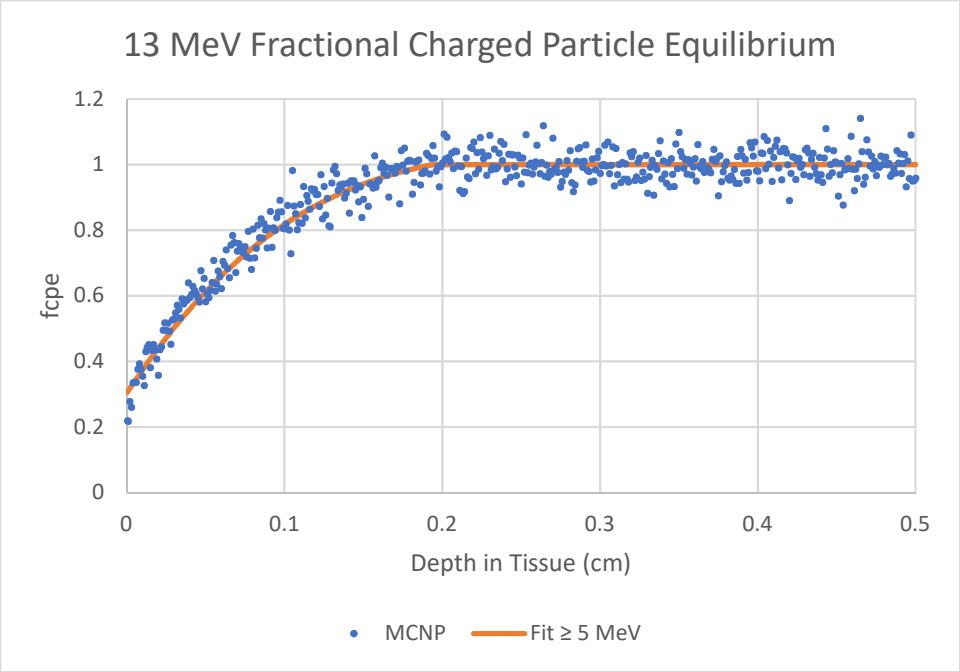

Figure A. 29: Fractional Charged Particle Equilibrium at 13 MeV

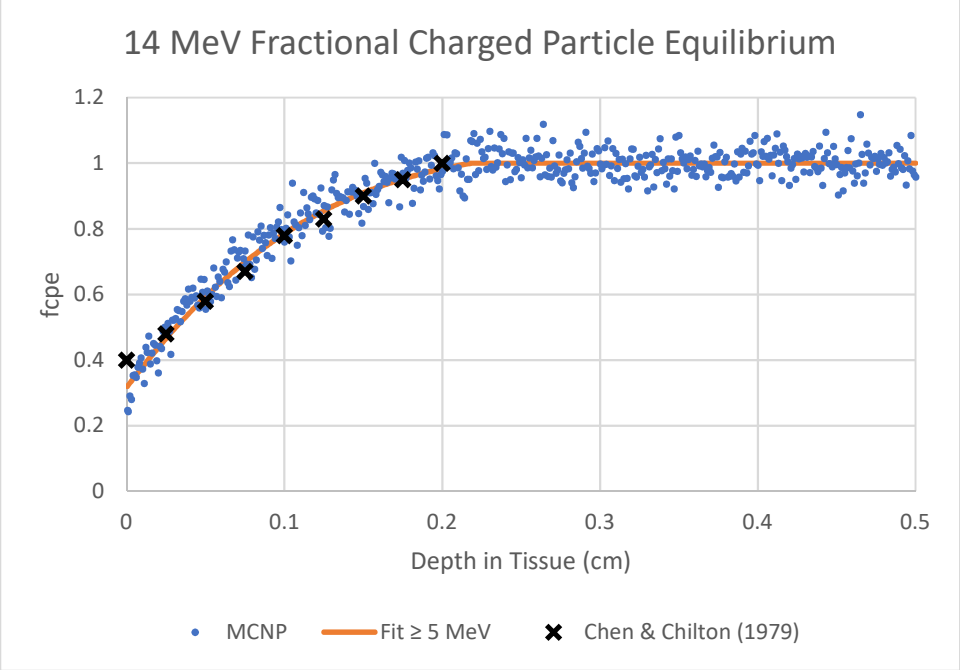

Figure A. 30: Fractional Charged Particle Equilibrium at 14 MeV

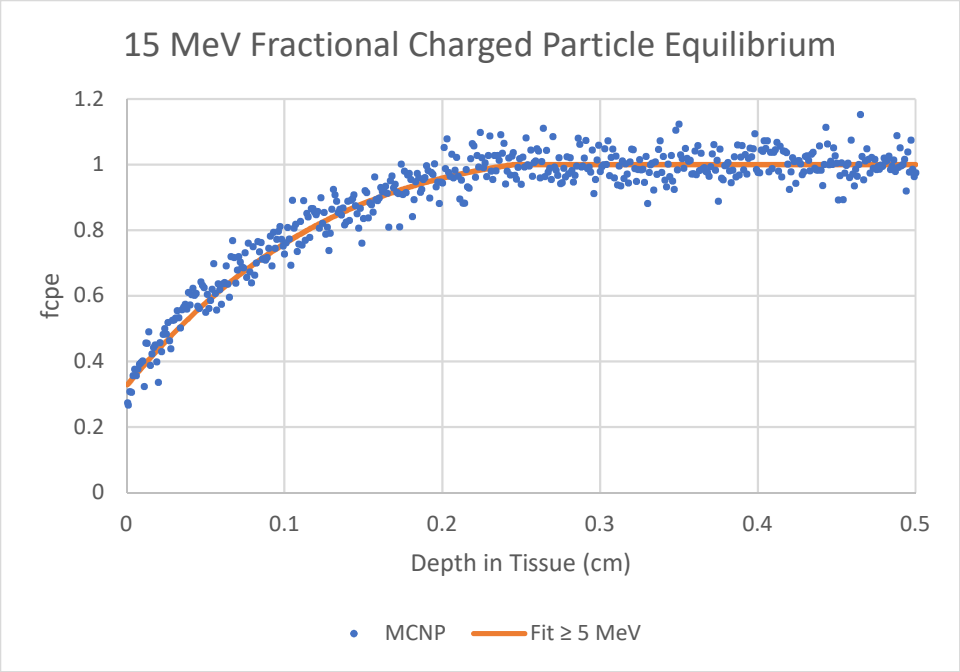

Figure A. 31: Fractional Charged Particle Equilibrium at 15 MeV

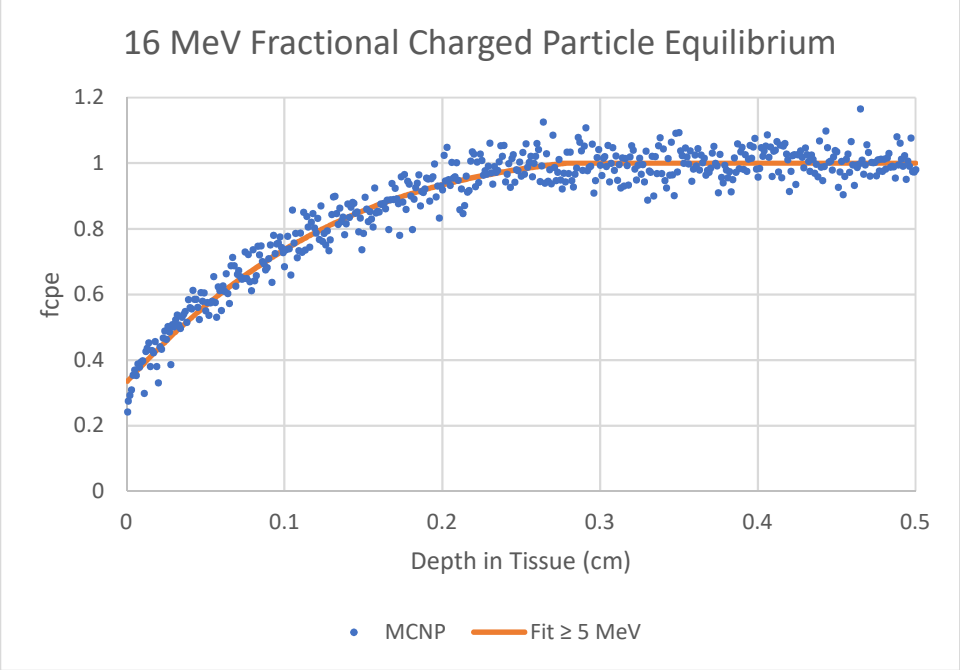

Figure A. 32: Fractional Charged Particle Equilibrium at 16 MeV

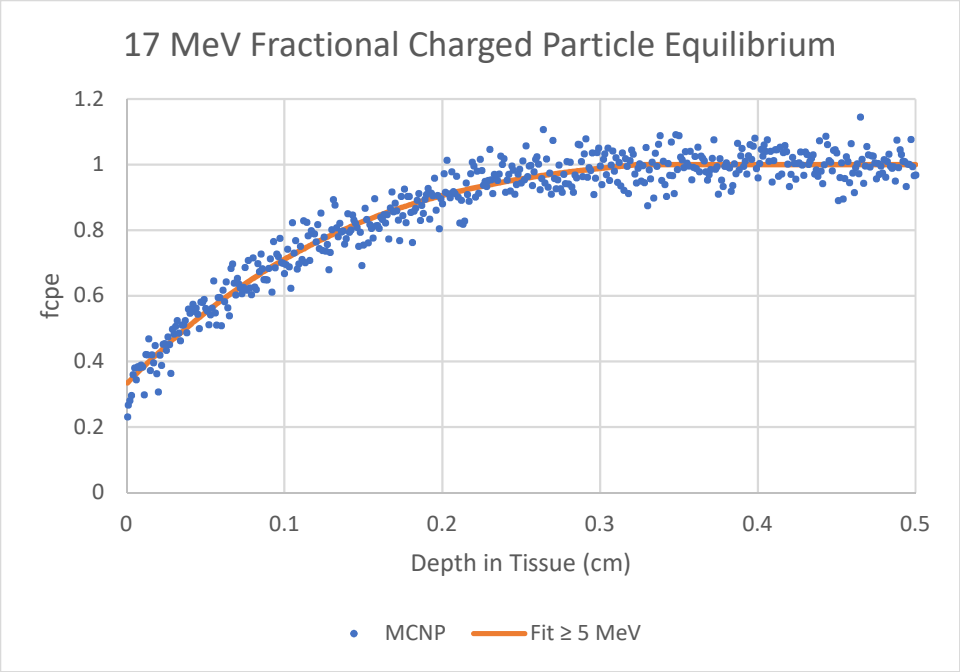

Figure A. 33: Fractional Charged Particle Equilibrium at 17 MeV

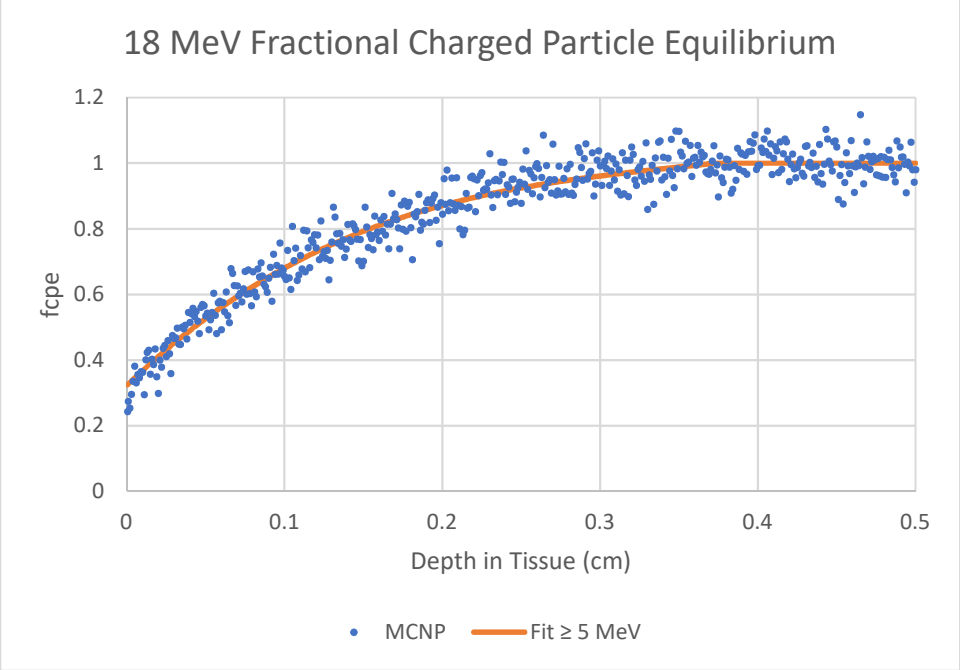

Figure A. 34: Fractional Charged Particle Equilibrium at 18 MeV

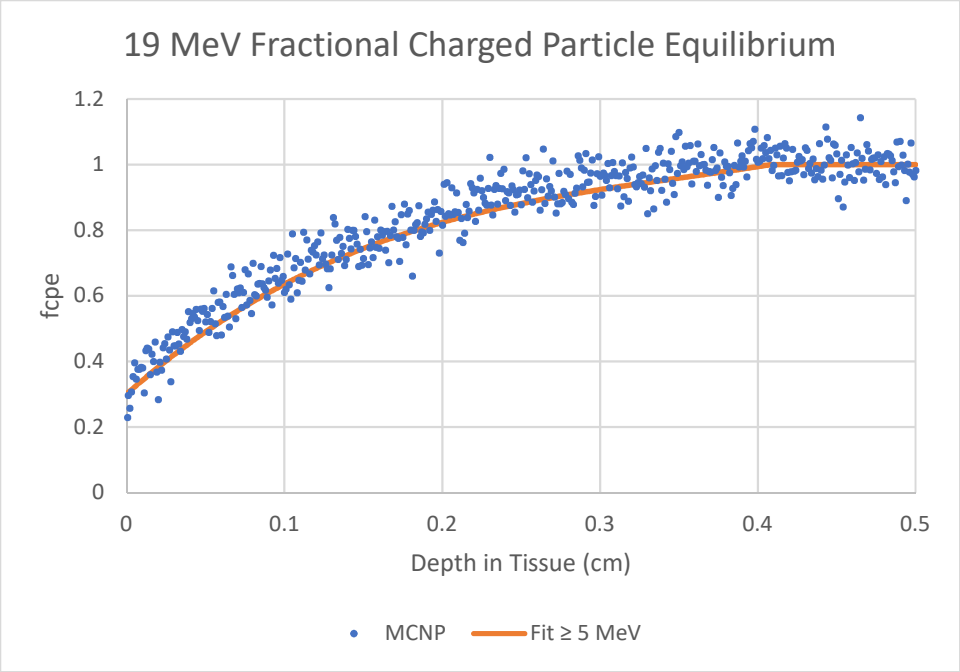

Figure A. 35: Fractional Charged Particle Equilibrium at 19 MeV

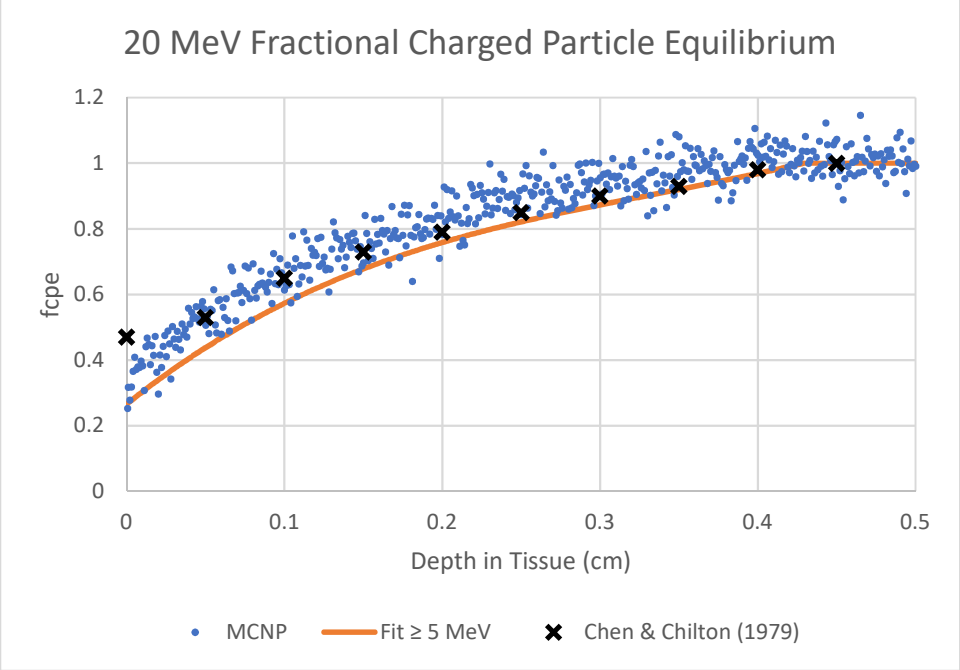

Figure A. 36: Fractional Charged Particle Equilibrium at 20 MeV

Appendix C:MCNP Input

The following is an example of the MCNP input discussed in detail in chapter 3. It is meant to determine fractional charged particle equilibrium in 10-micron tissue segments exposed to a uniform parallel beam of neutrons. Within this simulation the only variable changing is that of the energy for neutron (*erg*). Due to the quantity of tissue segments utilized in this simulation, the cell and surface cards have been condensed for space.

```
Neutron Dose to Fragmented Soft Tissue Cylinder
C CELL CARDS**********************************
1     0      -1  11  -3  imp:p,e,h,n 1
2     0       2 -1113  -3  imp:p,e,h,n 1
3     0       1:-2:3     imp:p,e,h,n 0
4     1   -1   4  -3  1113  -11      imp:p,e,h,n 1
11       1         -1        -11       12        -4        imp:p,e,h,n 1
12       1         -1        -12       13        -4        imp:p,e,h,n 1
13       1         -1        -13       14        -4        imp:p,e,h,n 1
14       1         -1        -14       15        -4        imp:p,e,h,n 1
.
.         Condensed for Space
.
1110    1         -1        -1110   1111    -4        imp:p,e,h,n 1
1111    1         -1        -1111   1112    -4        imp:p,e,h,n 1
1112    1         -1        -1112   1113    -4        imp:p,e,h,n 1

C SURFACE CARDS**********************************
1        py  4
2        py -10
3        cy  10
4        cy  1.78412412
11        py        0
12        py        -0.0005
13        py        -0.0015
14        py        -0.0025
15        py        -0.0035
.
.         Condensed for Space
.
1110    py        -1.0985
1111    py        -1.0995
1112    py        -1.1005
1113    py        -1.1015

C SOURCE CARD************************************************
mode     p e h n
sdef     par n erg 15 pos 0 2 0 ext 0 rad d1 axs 0 1 0 vec 0 -1 0 dir 1
si1      0 1.78412412
sp1      -21 1
c ICRU 4 COMPONENT SOFT TISSUE MATERIAL DEFINITION *********
m1   1001    -0.101172
       6000    -0.111000
       7014    -0.026000
       8016    -0.761828
FC6 Kerma (Gy) ***********************************************
```

```
fm6  1.60217662E-10
+f6  11 12      13      14      15      16      17      18      19      20
        21      22      23      24      25      26      27      28      29      30
        .
        .       Condensed for Space
        .
        1001    1002    1003    1004    1005    1006    1007    1008    1009    1010
        1111    1112
FC8                     ABSORBED                        DOSE                    (Gy)
**********************************************************
*f8:n 11        12      13      14      15      16      17      18      19      20
        21      22      23      24      25      26      27      28      29      30
        .
        .       Condensed for Space
        .

        1001    1002    1003    1004    1005    1006    1007    1008    1009    1010
        1111    1112
nps     5E6
```